CHAPTER 1

The Mesoscale

The prefix *meso*- comes from the Greek *mesos*, meaning “intermediate” or “in the middle.” Materials scientists and engineers describe the structure of a substance at four different length scales: macroscopic > mesocopic > microscopic > molecular/ nano level. Sometimes the labels for the two intermediate levels are interchanged. To avoid confusion in this textbook, we group these two levels into one “meso” length scale between the nano- and macroscopic levels.

Before the advent of X-ray diffractometry, mineralogists could only visually examine crystals. An entire classification scheme was developed and still in use today for describing a single crystal’s external morphology, or macroscopic appearance. One or more of 47 possible *forms* are usually apparent in the morphology. A form is a collection of symmetry-equivalent faces. The crystal *habit*, which depends on the relative sizes of the faces of the various forms present, may be described as cubic, octahedral, fibrous, acicular, prismatic, dendritic (tree-like), platy, or blade-like, among others. If a crystal is grown in a symmetrical environment, for example, freely suspended in a liquid, its morphological symmetry is exactly that of the point group *isogonal* (same angular relation) with its space group. It will depart from true point group symmetry under nonsymmetrical growth conditions.

With conventionally processed polycrystals, the smallest particles that are discernible with a high-quality optical microscope are the individual crystallites, or grains, that make up the sample. The term *microstructure* refers to the grain morphology, or grain size, shape, and orientation. Different techniques may be used to examine specific structural features. For example, high-resolution imaging with a scanning electron microscope (SEM) enables observation of dislocations. Information about preferred orientation can be obtained with an X-ray diffractometer equipped with a texture goniometer or by electron backscattered diffraction (EBSD).

Given the penetration depths in Table 1.1, it is obvious that electron diffraction and microscopy only probe the surfaces of solids (the topmost atomic layers), whereas neutron and X-ray diffraction provide information about the bulk. It is well known that the surface crystalline structure of a solid may differ from that of the bulk. The surfaces of most samples, however, are usually subjected to some sort of

---

Principles of Inorganic Materials Design By John N. Lalena and David A. Cleary
ISBN 0-471-43418-3

TABLE 1.1 Some Probes Used in Materials Characterization

Source	Wavelength[a] (Å)	Penetration Depth
Light	4×10^3–7×10^3	0
Neutrons	1–2.5	cm–dm
X-rays	0.1–10	μm–mm
Electrons	0.04	nm

[a] For elementary particles, $\lambda = hc/\sqrt{(2mc^2E)}$; for light and X-rays, $\lambda = hc/E$.

chemical–mechanical polishing prior to microstructural analysis to ensure that bulk grain morphology is apparent.

Inorganic materials are commonly grouped into one of two structure categories: crystalline or amorphous (glassy). Amorphous materials possess no long-range structural order, or periodicity. By contrast, crystalline solids are composed of arrays of atoms or molecules, whose positions may be referenced to a translationally invariant lattice. All crystals possess one or more of the basic symmetry elements. Some authors also classify fractals as a distinct structural class. In this case, the structure is self-similar, or scale-invariant, looking identical at all length scales (e.g., cauliflowers and silica aerogels). Crystal structure, however, is the topic of the next chapter. In this chapter, we focus on the microstructures of polycrystalline solids. The majority of solid materials of technological interest are used in polycrystalline form.

Microstructure is determined by the conditions used during the material processing. Hence, our objective is to clarify that a major goal of inorganic materials engineering is the systematic generation of specific grain morphologies in order to vary and adapt the properties of polycrystalline materials to given applications. We focus on describing the microstructures of solidification products (metals), formed powder aggregates (ceramics), and thin films. Microstructure/property correlation is also discussed. Mechanical, chemical, and transport properties are markedly influenced by microstructure.

1.1 INTERFACES IN POLYCRYSTALS

The regions separating different grains, or crystallites, within a polycrystalline solid are called *grain boundaries*. Although grain boundaries are often regarded as regions of structural disorder, it is now well established that many have a periodic structure. True incoherency, in which there is little correlation between atomic positions across the boundary, only sets in when the mismatch between adjacent crystals is very high (Bhadeshia, 1987). This is primarily determined by the relative orientations of the adjoining grains. In a polycrystalline sample, both the grain orientation distribution, or *texture*, and the structure of the grain boundary itself can be crucial to the bulk materials properties. Therefore, it is appropriate to begin with orientation relationships.

1.1.1 Orientation Relationships in Bicrystals

The orientation relationship between a pair of grains of the same substance (the only kind we will consider here), a *bicrystal*, is often expressed by an axis-angle description, since one crystal always can be generated from the other by a rigid-body rotation about a suitable axis. More precisely, the lattices can be made to coincide by turning one of the crystals about a suitable rotation axis. Rotation axes are commonly denoted as unit vectors, in terms of three indices of direction written in square brackets, [*uvw*], while the misorientation angle is expressed in degrees about this axis. The [*uvw*] indices are obtained by taking the projections of the vector on the x, y, and z-axes, respectively, of a Cartesian coordinate system and dividing these three numbers by their highest common denominator.

It is always possible to describe the orientation relationship between a pair of grains in terms of more than one axis-angle pair. Consider a pair of adjacent identical cubic crystals of different orientation, A and B. Suppose further that B can be generated from A by a right-hand rotation of 60° counterclockwise about the A crystal's body-diagonal axis, or the $[111]_A$ direction. This particular orientation relationship is called a *twin*, since the two domains are related by a symmetry element (a twin operation) that is not part of the space group symmetry of a single crystal of the material. The extra symmetry element may be a reflection plane (twin plane) or a rotation axis (twin axis). The high symmetry of the cubic lattice allows us to find numerous equivalent axis-angle pairs for any orientation relationship. Using this twin boundary as an example, we now show how other axis-angle pairs, which are equivalent to a 60° right-hand rotation about the $[111]_A$ axis, can be obtained.

Indices are convenient for describing directions (vectors or axes) in crystals. However, direction cosines are much more useful for calculations. Therefore, one must first convert the direction indices, [*uvw*], designating the rotation axis into direction cosines. In our present example, the body diagonal of a cube of unit length has direction indices [111]. This is seen by using a Cartesian coordinate system, where the origin of the cube is taken to be one of its corners and which is designated as $(x_1, y_1, z_1) = (0, 0, 0)$. The body diagonal is obtained by drawing a line segment of length $|\boldsymbol{r}|$ from the origin and terminating at the coordinates $(x_2, y_2, z_2) = (1, 1, 1)$. The direction cosines are given by the equations:

$$\begin{aligned} \cos\alpha &= r_1 = (x_2 - x_1)/\,|\,\boldsymbol{r}\,| \\ \cos\beta &= r_2 = (y_2 - y_1)/\,|\,\boldsymbol{r}\,| \\ \cos\gamma &= r_3 = (z_2 - z_1)/\,|\,\boldsymbol{r}\,| \end{aligned} \tag{1.1}$$

where $|\boldsymbol{r}|$ is given by $[r_1^2 + r_2^2 + r_3^2]^{1/2} = [(x_2 - x_1)^2 + (y_2 - y_1)^2 + (z_2 - z_1)^2]^{1/2}$. Hence, in the cubic crystal, we get $\cos\alpha = \cos\beta = \cos\gamma = 0.5773$, satisfying the requirement that $\cos^2\alpha + \cos^2\beta + \cos^2\gamma = 1$.

A (3 × 3) square rotation matrix, **R**, may now be obtained, which has the following elements:

$$\begin{pmatrix} r_1 r_1(1-\cos\theta)+\cos\theta & r_1 r_2(1-\cos\theta)+r_3\sin\theta & r_1 r_3(1-\cos\theta)-r_2\sin\theta \\ r_1 r_2(1-\cos\theta)-r_3\sin\theta & r_2 r_2(1-\cos\theta)+\cos\theta & r_2 r_3(1-\cos\theta)+r_1\sin\theta \\ r_1 r_3(1-\cos\theta)+r_2\sin\theta & r_2 r_3(1-\cos\theta)-r_1\sin\theta & r_3 r_3(1-\cos\theta)+\cos\theta \end{pmatrix} \tag{1.2}$$

In this book, we follow the standard convention for all matrices, that the elements a_{i1}, $a_{i2}, \ldots, a_{in}$ are the elements of the ith row, and the elements $a_{1j}, a_{2j}, \ldots, a_{mj}$ are the elements of the jth column. That is, the first subscript for an element denotes the column and the second subscript gives the row. Equation 1.2 transforms the components of a vector referred to one basis to those referred to the other basis as:

$$\begin{aligned} a_1 &= R_{11}b_1 + R_{21}b_2 + R_{31}b_3 \\ a_2 &= R_{12}b_1 + R_{22}b_2 + R_{32}b_3 \\ a_3 &= R_{13}b_1 + R_{23}b_2 + R_{33}b_3 \end{aligned} \tag{1.3}$$

In Eq. 1.3, R_{23}, for example, is the second element in the third row (or, equivalently, the third element of the second column) of Eq. 1.2. For $r_1 = r_2 = r_3 = 0.5773$ and $\theta = 60°$, Eq. 1.2 gives:

$$\mathbf{R} = \begin{pmatrix} 0.6667 & 0.6667 & 0.3333 \\ -0.3333 & 0.6667 & 0.6667 \\ 0.6667 & 0.3333 & 0.6667 \end{pmatrix} \tag{1.4}$$

In order to obtain the equivalent axis-angle pairs, **R** must be multiplied by the matrices representing the 24 rotation operations of the cubic lattice. The rotational degeneracy of all crystal lattices can be obtained from the character tables for their respective point groups: cubic, O_h (24), hexagonal, D_{6h} (12), hexagonal close packed, D_{3d} (6), tetragonal, D_{4h} (8), trigonal, D_{3d} (6), orthorhombic, D_{2h} (4), monoclinic, C_{2h} (2), and triclinic, C_i (1).

Continuing with the present example, we can operate on Eq. 1.4 with the (3 × 3) square matrix representing, say, a 90° right-hand rotation about [100], which is obtained from Eq. 1.2 with $r_1 = 1$, $r_2 = r_3 = 0$ and $\theta = 90°$. The result is a product matrix, which we call **J**:

$$\begin{aligned} \mathbf{J} &= \begin{pmatrix} 1 & 0 & 0 \\ 0 & 0 & 1 \\ 0 & -1 & 0 \end{pmatrix} \begin{pmatrix} 0.6667 & 0.6667 & -0.3333 \\ -0.3333 & 0.6667 & 0.6667 \\ 0.6667 & -0.3333 & 0.6667 \end{pmatrix} \\ &= \begin{pmatrix} 0.6667 & 0.6667 & -0.3333 \\ 0.6667 & -0.3333 & 0.6667 \\ 0.3333 & -0.6667 & -0.6667 \end{pmatrix} \end{aligned} \tag{1.5}$$

Note that **J** is *not* the product of two symmetry operations, because the first rotation took crystal A into crystal B, rather than back into itself. The A and B orientations are distinguishable. We can now use **J** to extract an equivalent axis-angle pair. The new rotation angle, θ, is given by

$$j_{11} + j_{22} + j_{33} = 1 + 2\cos\theta \tag{1.6}$$

where the terms on the left-hand side are the diagonal elements of **J**. The equivalent rotation axis for $\theta \neq \pi$ or, for nonsymmetric matrices (when ${}^t\mathbf{J} \neq \mathbf{J}$), is obtained from the relations:

$$r_1 = [j_{23} - j_{32}]/2\sin\theta, \qquad r_2 = [j_{31} - j_{13}]/2\sin\theta, \qquad r_3 = [j_{12} - j_{21}]/2\sin\theta \tag{1.7}$$

where $r_1^2 + r_2^2 + r_3^2 = 1$. When the product matrix is symmetric (${}^t\mathbf{J} = \mathbf{J}$), for example, if $\theta = 180°$, Eq. 1.6 does not apply. In this case, the following equation is needed to determine the rotation matrix:

$$\begin{array}{lll} j_{11} = 1 - 2(r_2^2 + r_3^2) & j_{12} = 2r_1r_2 & j_{13} = 2r_1r_3 \\ j_{21} = 2r_1r_2 & j_{22} = 1 - 2(r_1^2 + r_3^2) & j_{23} = 2r_2r_3 \\ j_{31} = 2r_1r_3 & j_{32} = 2r_2r_3 & j_{33} = 1 - 2(r_1^2 + r_2^2) \end{array} \tag{1.8}$$

where $r_1^2 + r_2^2 + r_3^2 = 1$. When using Eq. 1.8, the idea is to extract the maximum component from the diagonal elements of the matrix. If j_{11} is of maximum magnitude, compute:

$$r_1 = [j_{11} - j_{22} - j_{33} + 1]^{1/2}/2 \qquad r_2 = j_{13}/2r_1 \qquad r_3 = j_{13}/2r_1$$

If j_{22} is the maximum, compute:

$$r_2 = [j_{22} - j_{11} - j_{33} + 1]^{1/2}/2 \qquad r_1 = j_{12}/2u_2 \qquad r_3 = j_{23}/2r_2$$

If j_{33} is the maximum, compute:

$$r_3 = [j_{33} - j_{11} - j_{22} + 1]^{1/2}/2 \qquad r_1 = j_{13}/2r_3 \qquad r_2 = j_{23}/2r_3$$

Example 1.1 Calculate the axis-angle pair from the product matrix in Eq. 1.5 that is equivalent to a 60° rotation about $[111]_A$.

Solution The rotation angle, using Eq. 1.6, is

$$\cos^{-1}([0.6667 - 0.3333 - 0.6667 - 1]/2) = \theta = 2.300\,\text{rad}$$
$$2.3000 \times 180/\pi = 131.8°$$

TABLE 1.2 Axis-Angle Pairs Equivalent to a 60° Rotation about $\langle 111\rangle_A$ in a Cubic Bicrystal

Axis	Angle
$\langle 111\rangle_A$	180°
$\langle 012\rangle_A$	131.8°
$\langle 112\rangle_A$	180°
$\langle 113\rangle_A$	146.4°
$\langle 11\bar{\mathbf{3}}\rangle_A$	146.4°
$\langle 011\rangle_A$	70.5°
$\langle 011\rangle_A$	109.5°

We see by inspection that **J** is a nonsymmetric matrix $(j_{ij} \neq j_{ji})$. Therefore, we can use Eq. 1.7 to compute the components of the rotation axis:

$$r_1 = [0.6667 - (-0.6667)]/2\ \sin(131.8) = 0.8943$$
$$r_2 = [0.3333 - (-0.3333)]/2\ \sin(131.8) = 0.4470$$
$$r_3 = [0.6667 - 0.6667]/2\ \sin(131.8) = 0$$

From vector algebra, we know that any ordered set of three numbers that can be obtained from $[r_1\ r_2\ r_3]$ by multiplying all of them by the same positive constant k is also a set of direction numbers for the vector $\boldsymbol{r}$, in that they define the direction of the vector. Hence choosing k to be (1/0.4470) gives: [0.8943/0.4470, 0.4470/0.4470, 0] or [210]. Therefore, the equivalent axis-angle pair is rotated by 131.8° about $[210]_A$.

Using the procedure just outlined with other symmetry operations of the cubic lattice, we can calculate other axis-angle pairs that, for the purposes of expressing the orientation relationship in a cubic bicrystal, are equivalent to a 60° rotation about $\langle 111\rangle_A$. The results are given in Table 1.2

Obviously, a completely unambiguous description of the relative orientation between two identical crystals must contain the axis-angle pair (rather than an angle alone). As we have just seen, however, a rotation matrix can also be used to specify the orientation relation within a bicrystal. We have just gone to great lengths to show how these matrix elements are computed. The advantage of expressing the orientation relationship in this manner will be apparent in Section 1.1.3 where we quantify the "goodness of fit" at the interface between grains.

1.1.2 Grain Boundary Orientations

We have been discussing orientation relationships between pairs of grains. This is *not* the same as the orientation of the grain boundary. For example, Figure 1.1 shows a twinned bicrystal like that discussed earlier. As illustrated in the figure, the grain boundary plane between two crystals with this orientation relationship need not coincide with the twin plane. The orientation relationship between the grains

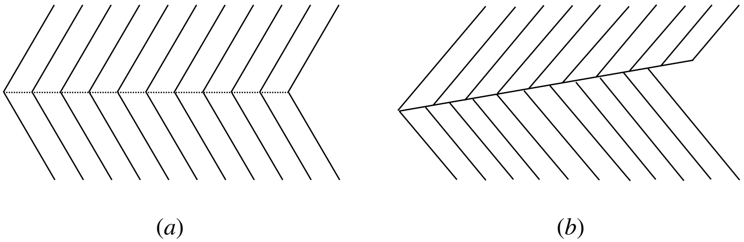

Figure 1.1 (a) The twin plane coincides with the boundary plane. (b) The twin plane and boundary plane do not coincide.

does provide us with three of the five degrees of freedom needed to specify the grain boundary orientation, however. One of these degrees of freedom, we have seen, is a rotation angle. The rotation is carried out about a rotation axis, which we have been denoting by three indices of direction, [*uvw*]. Because an axis is a polar vector in spherical coordinates, it can also be specified by a polar angle and an azimuthal angle relative to the grain boundary plane. Thus, three of our five degrees of freedom are Euler angles that, taken together, describe the orientation relationship between the grains: $0 \leq \phi_E \leq 2\pi$; $0 \leq \theta_E \leq \pi$; and $0 \leq \psi_E \leq 2\pi$ (the subscript E simply denotes that these are Euler angles). The remaining two degrees of freedom define the boundary plane in the coordinate system of the reference grain. They are spherical angles that specify the boundary plane inclination: $0 \leq \theta_S \leq 2\pi$; $0 \leq \phi_S \leq \pi$, where the subscript S denotes spherical angles.

One might naturally ask: How many different grain boundary orientations are observable? The number of distinguishable orientations, N, depends on the precision with which the various angular measurements are made, and the number of symmetry operators for the crystal class. For example, for a cubic bicrystal the boundary normal can be selected in two directions, the crystals can be exchanged, and one can apply 24 rotation operations to either crystal. There are thus $2 \cdot 2 \cdot 24^2$ combinations of the five angular parameters that lead to identical bicrystals. To generalize, if we represent the number of symmetry operations for the crystal class by η, the precision of the angular measurements by Δ, and the number of degrees of freedom by n, we have the following formula for the number of distinguishable orientations (Saylor et al., 2000).

$$\begin{aligned} N &= 1/(4\eta^2)\prod_{n,\Delta}(n/\Delta) \\ &= [(2\pi)(\pi)(2\pi)(2\pi)(\pi)]/(4\eta^2\Delta^5) \\ &= 8\pi^5/(4\eta^2\Delta^5) \end{aligned} \tag{1.9}$$

where Δ is in radians. The $8\pi^5$ factor is the product of the full ranges for each angular parameter. For a cubic system, if $\Delta = 0.087$ (5°), Eq. 1.9 predicts 2.1×10^5 distinct boundaries. The number of distinguishable boundaries obviously increases with increases in the angular precision.

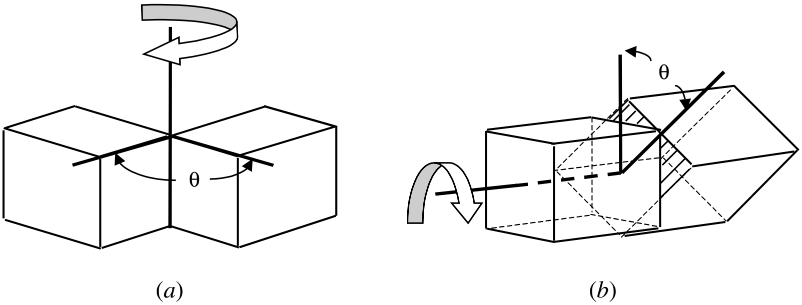

Figure 1.2 (a) A tilt boundary. (b) A twist boundary.

Despite such a large number of possible orientations, it has been observed experimentally that grain orientation relationships do not occur in a random manner. For example, low-energy grain boundaries like the twin boundary are very commonly observed in cubic systems. It is hard to say whether this is a result of thermodynamic or kinetic control. Interfacial energy minimization could be responsible, or the activation energies for nucleation and grain growth in certain orientations could be lower, or possibly both factors could be at work.

The Dislocation Model of Low Angle Grain Boundaries A general grain boundary has a mixture of *tilt* and *twist* character. We can think of a pure tilt boundary as consisting of an axis of rotation that is in the grain boundary plane (Figure 1.2a). In contrast, twist boundaries contain an axis of rotation that is perpendicular to the grain boundary plane (Figure 1.2b). A useful way to picture the symmetrical tilt boundary (a boundary in which the boundary plane contains the rotation axis and bisects the rotation angle) is to consider it as a straight array of *edge dislocations*, as in Figure 1.3. In a single-crystal metal, edge dislocations consist of extra half-planes of atoms. In ionic or covalent crystals, edge dislocations involve extra half planes of unit cells. As long as the misorientation angle is low (i.e., small-angle grain boundaries), tilt boundaries may be regarded as the coalescence of these line defects into a dislocation network. The spacing between the dislocations, D, is

$$D = \boldsymbol{b}/\sin\theta \tag{1.10}$$

where $\boldsymbol{b}$ is the *Burgers vector*, perpendicular to the line of the dislocation, and θ is the misorientation angle.

If the dislocation density is low (the value of D is large), a semicoherent interface results, in which regions of good fit are separated by the individually recognizable interface dislocations. Note how the extra half-planes in Figure 1.3 all have a single Burgers vector. In an unsymmetrical low-angle tilt boundary, different Burgers vectors are required to accommodate the mismatch. The dislocation model is really only valid for low-angle grain boundaries. In the cubic crystal class, for

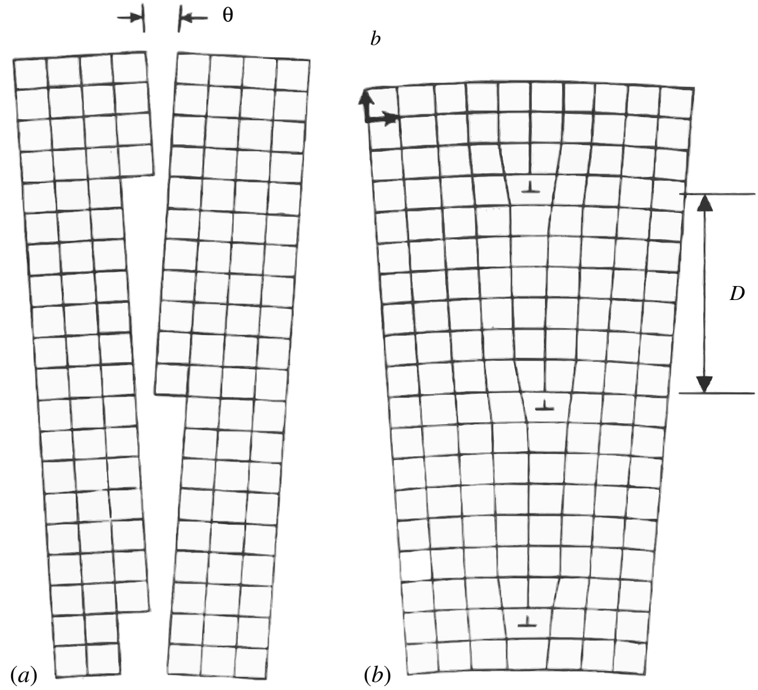

Figure 1.3 (a) A low-angle tilt boundary. (b) Representation as an array of parallel edge dislocations.

values θ >∼15°, *D* can get so small, corresponding to a high dislocation density, that dislocations become indistinguishable (Read and Shockley, 1950). The symmetrical low-angle twist boundary can similarly be represented by a screw dislocation (Figure 1.4). Screw dislocations have been likened to multistoried parking garages, the atomic planes spiraling around the dislocation line in the same

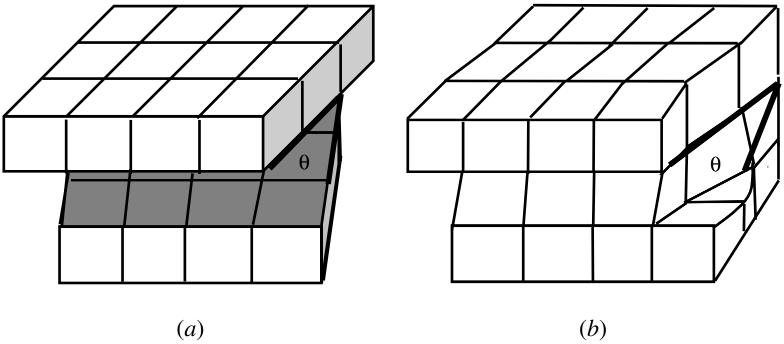

Figure 1.4 (a) A low-angle twist boundary. (b) Representation as a screw dislocation.

manner as a parking garage floor spirals around a central pole of the garage (Weertman and Weertman, 1992).

1.1.3 Grain Boundary Geometry: The Coincidence Site Lattice

The evolution of our modern picture of crystalline interfaces can be summarized as follows. The earliest geometric models of crystalline interfaces were the "amorphous" high-angle grain boundary by Hargreaves and Hill (Hargreaves and Hill, 1929), and the twin interface by the French mining engineer and crystallographer Georges Friedel (1865–1933) (Friedel, 1926), son of organic chemist Charles Friedel. (1832–1899). N. F. Mott first suggested that grain boundaries should contain regions of fit and misfit (Mott, 1948). Kronberg and Wilson then pointed out the importance of the coincidence of atom positions across grain boundaries in influencing metal properties such as diffusion coefficients and mobilities (Kronberg and Wilson, 1949). Ranganthan presented a general procedure for obtaining coincidence relationships between lattices about rotation axes (Ranganathan, 1966).

The modern method for quantifying the goodness of fit between two adjacent grains examines the number of lattice points (*not* atomic positions) from each grain that coincide. In special cases, for example when the grain boundary plane is a twin plane, the lattice sites for each of the adjacent crystals coincide *in* the boundary. These are called *coherent* boundaries. It has long since been experimentally verified that coherent grain boundaries possess special properties. For example, coherent boundaries migrate faster than random boundaries during recrystallization (Aust and Rutter, 1959).

Consider a pair of adjacent crystals. We mentally expand the two neighboring crystal lattices until they interpenetrate and fill all space. Without loss of generality, it is assumed that the two lattices possess a common origin. If we now hold one crystal fixed and rotate the other, it is found that a number of lattice sites for each crystal, in addition to the origin, coincide with certain relative orientations. The set of coinciding points form a *coincidence site lattice*, or CSL, which is a sublattice for both the individual crystals.

In order to quantify the lattice coincidence between the two grains, A and B, the symbol Σ customarily designates the reciprocal of the fraction of A (or B) lattice sites that are common to both A and B.

$$\Sigma = \text{Number of crystal lattice sites/Number of coincidence lattice sites} \qquad (1.11)$$

For example, if one-third of the A (or B) crystal lattice sites are coincidence points belonging to both the A and B lattices, then, $\Sigma = 1/(1/3) = 3$. The value of Σ also gives the ratio between the areas enclosed by the CSL unit cell and crystal unit cell. The value of Σ is a function of the lattice types and grain misorientation. The two grains need not have the same crystal structure or unit cell parameters. Hence, they need not be related by a rigid-body rotation. The boundary plane intersects the CSL and will have the same periodicity as that portion of the CSL along which the intersection occurs.

The simple CSL model is directly applicable to the cubic crystal class. The lower symmetry of the other crystal classes necessitates the more sophisticated formalism known as the *constrained coincidence site lattice*, or CCSL (Chen and King, 1988). In this book, we only treat cubic systems. Interestingly, whenever an *even* value is obtained for Σ in a cubic system, it will always be found that an additional lattice point lies in the center of the CSL unit cell. The true area ratio is then half the apparent value. This operation can always be applied in succession, until an odd value is obtained—thus Σ is always *odd* in the cubic system. A rigorous mathematical proof of this would require that we invoke what is known as O-lattice theory (Bollman, 1967) The O-lattice takes into account all equivalence points between two neighboring crystal lattices. It includes as a subset not only coinciding lattice points (the CSL) but also all nonlattice sites of identical internal coordinates. However, to expand on that topic would be well beyond the scope of this textbook. The interested reader is referred to Bhadeshia (1987) or Bollman (1970).

Single crystals and bicrystals with no misorientation (i.e., $\theta = 0$), by convention, are denoted Σ1. In practice, small- or low-angle grain boundaries with a misorientation angle less than 10°–15° are also included under the Σ1 term. Since Σ is always odd, the coincidence orientation for high-angle boundaries with the largest fraction of coinciding lattice points is Σ3 (signifying that 1/3 of the lattice sites coincide). Next in line would be Σ5, then Σ7, and so on.

Figure 1.5 shows a tilt boundary between two cubic crystals. The grain boundary plane is perpendicular to the plane of the page. In the figure, we are looking down one of the $\langle 100\rangle$ directions, and the [100] axis about which grain *B* is rotated is also perpendicular to the page and passes through the origin. At the precise misorientation angle of 36.9°, one-fifth of the *B* crystal lattice sites are coincidence points, which also belong to the expanded lattice of crystal *A*; this is a Σ5 CSL misorientation. The set of coincidence points forms the CSL, the unit cell of which is outlined. Note that the area enclosed by the CSL unit cell is five times that enclosed by the crystal unit cell.

Fortunately, there is an easy, although tedious, way to determine the true value for Σ. If an integer, *N*, can be found such that all the elements of the rotation matrix become integers when multiplied by *N*, then that integer will be the Σ value. The value of *N* is found simply by multiplying all the matrix elements by integers, in increments of one beginning with the number 1, until the matrix elements are all integers. If the value of Σ turns out to be even using this procedure, then the true value is obtained by successively dividing *N* by two until the result is an odd integer. This method can be used to compute the value of Σ for any general rotation matrix. For example, factoring out 1/3 from **R** in Eq. 1.4 gives a matrix with integral elements, in which Σ is equal to three:

$$\mathbf{R} = 1/3\begin{pmatrix} 2 & 2 & -1 \\ -1 & 2 & 2 \\ 2 & -1 & 2 \end{pmatrix}$$

Hence, the 60° $\langle 111\rangle$ twin boundary has a Σ3 CSL misorientation. It is also a coherent boundary because of the large number of coincidence points along the

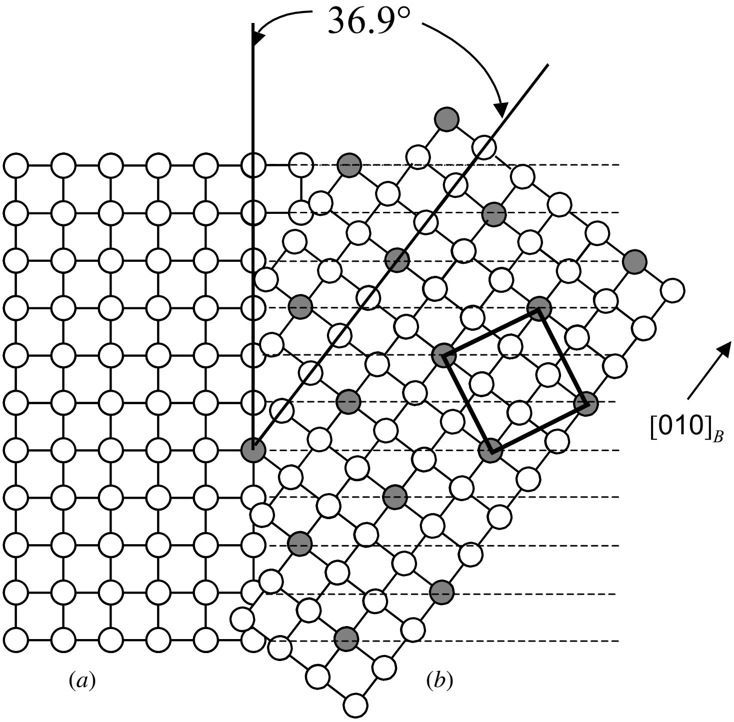

Figure 1.5 A view down the [001] direction of a tilt boundary between two crystals (*A*, *B*) with a misorientation angle of 36.9° about [001]. The grain boundary is perpendicular to the plane of the page. Every fifth atom in the [010] direction in *B* is a coincidence point (shaded). The area enclosed by the CSL unit cell (bold lines) is five times that of the crystal unit cell, so $\Sigma = 5$.

twin plane itself, as shown in Figure 1.6. In this figure, we are looking down *on* the $\langle 111\rangle$ rotation axis. The lattice sites shown are in rows off the $\langle 111\rangle$ axis, along the set of (111) planes, as illustrated in the bottom left corner. It will be recalled that the boundary plane intersects the CSL and will have the same periodicity as that portion of the CSL along which the intersection occurs. Thus, not all $\Sigma 3$ boundaries will be coherent. For example, although rotations of 70.5° and 109.5° about $\langle 011\rangle_A$ are also equivalent $\Sigma 3$ misorientations, only the 70.5° rotation will result in a high degree of coincidence along the $\langle 011\rangle$.

Example 1.2 The matrix corresponding to a rotation of 50.5° about [110] is given in Bhadeshia's monograph *Worked Examples in the Geometry of Crystals* as:

$$\mathbf{R} = \begin{pmatrix} 0.545621 & -0.545621 & 0.636079 \\ 0.181961 & 0.818039 & 0.545621 \\ 0.818039 & 0.181961 & -0.545621 \end{pmatrix}$$

Calculate the value of Σ.

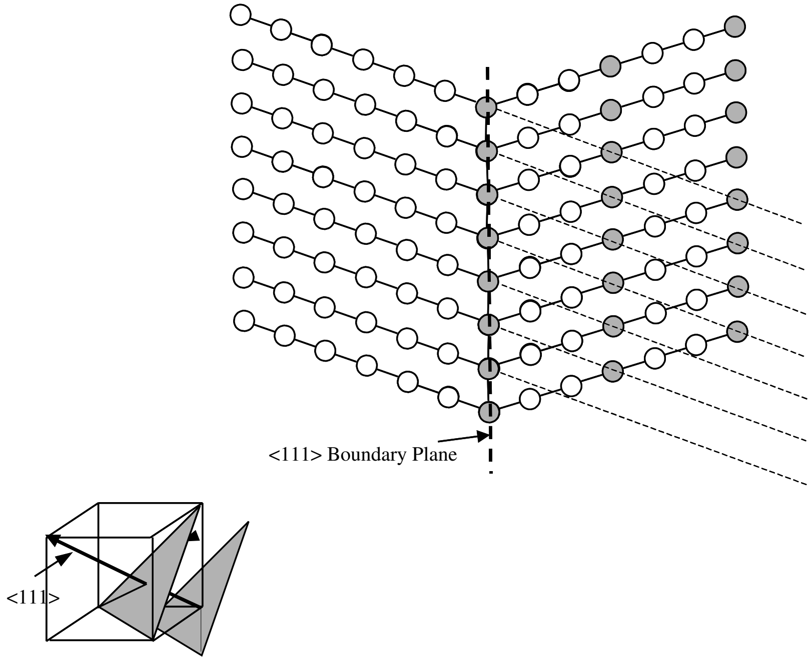

Figure 1.6 The twin boundary (perpendicular to the plane of the page) is a $\Sigma 3$ CSL misorientation. Note that there is complete coincidence in the boundary plane itself.

Solution Multiplying each matrix element by an integer, starting with the number 1, and progressing in increments of 1 until the products are integers shows that when $N = 11$, the rotation matrix can be written as

$$\mathbf{R} = 1/11 \begin{pmatrix} 6 & -6 & 6 \\ 6 & 9 & 6 \\ 9 & 2 & -6 \end{pmatrix}$$

Hence, $\Sigma = 11$.

For tilt boundaries, the value of Σ can also be calculated if the plane of the boundary is specified in the coordinate systems for both adjoining grains. This method is called the *interface-plane scheme* (Wolfe and Lutsko, 1989). In a crystal, lattice planes are imaginary sets of planes that intersect the unit cell edges (Section 2.1.3). These planes are denoted by Miller indices, a group of integers that are the reciprocals of the fractional coordinates of the points where the planes intercept each of the unit cell edges. In cubic crystals, the (*hkl*) planes are orthogonal to the [*uvw*] direction. The tilt and twist boundaries can be defined in terms of the Miller indices for each of the adjoining lattices and the twist angle, Φ, of both plane stacks normal to the boundary plane, as follows:

$(h_1k_1l_1) = (h_2k_2l_2); \Phi = 0$	symmetric tilt boundary
$(h_1k_1l_1) \neq (h_2k_2l_2); \Phi = 0$	asymmetric tilt boundary
$(h_1k_1l_1) = (h_2k_2l_2); \Phi > 0$	low-angle twist boundary
$(h_1k_1l_1) \neq (h_2k_2l_2); \Phi > 0$	high-angle twist boundary

Thus, the value of the CSL-Σ value is obtained for symmetric tilt boundaries between cubic crystals as follows:

$$\begin{aligned}\Sigma &= h^2 + k^2 + l^2 \qquad \text{for } h^2 + k^2 + l^2 = \text{odd} \\ &= (h^2 + k^2 + l^2)/2 \qquad \text{for } h^2 + k^2 + l^2 = \text{even}\end{aligned} \tag{1.12}$$

For asymmetric tilt boundaries between cubic crystals, Σ is calculated from (Randle, 1993):

$$\Sigma = [(h_1^2 + k_1^2 + l_1^2)/(h_2^2 + k_2^2 + l_2^2)]^{1/2} \tag{1.13}$$

For example, if we mentally expand the lattices of both A and B in Figure 1.5, it will be seen that the grain boundary plane cuts the B unit cell at (340) in the B coordinate system and the A unit cell at (010) in the A coordinate system. Thus, Eq. 1.13 yields $\Sigma = (25/1)^{1/2} = 5$.

In polycrystals, misorientation angles rarely correspond to *exact* CSL configurations. There are ways of dealing with this deviation, which set criteria for the proximity to an exact CSL orientation that an interface must have in order to be classified as belonging to the class $\Sigma = n$. The Brandon criterion (Brandon et al., 1964) asserts that the maximum permitted deviation is $v_0\Sigma^{-1/2}$. For example, the maximum deviation that a $\Sigma3$ CSL configuration with a misorientation angle of 15° is allowed to have and still be classified as $\Sigma3$ is $15°(3)^{-1/2} = 8.7°$. The coarsest lattice characterizing the deviation from an exact CSL orientation, which contains the lattice points for each of the adjacent crystals, is referred to as the displacement shift complete lattice (DSL).

Despite the difficulties associated with characterizing inexact CSL orientations, the CSL concept is useful because grain boundary structure, which depends on the orientation relationship between the grains and, hence, the CSL, directly influences intragranular properties like chemical reactivity (e.g., corrosion resistance), segregation, and fracture resistance. *Grain boundary engineering* is a relatively new field that concentrates on controlling the intragranular structure, or CSL geometry, to improve these properties, in turn, improving bulk materials performance (Watanabe, 1984, 1993). For the most part, this means introducing a large fraction of low-Σ boundaries, particularly twin boundaries. It is believed, however, that optimal grain boundary properties may be restricted to narrow regions (small deviations) about exact CSL orientations.

1.1.4 Grain Boundary Energy

A finite number of point defects (e.g., vacancies, impurities) can be found in any crystalline material because the configurational entropy term, $-T\Delta S$, for a low point-defect concentration outweighs the positive formation enthalpy in the free-energy expression, $\Delta G = \Delta H - T\Delta S$. Thus, introduction of a small number of point defects into a perfect crystal gives rise to a free-energy minimum, as illustrated in Figure 1.7a. Further increases in the point-defect concentration,

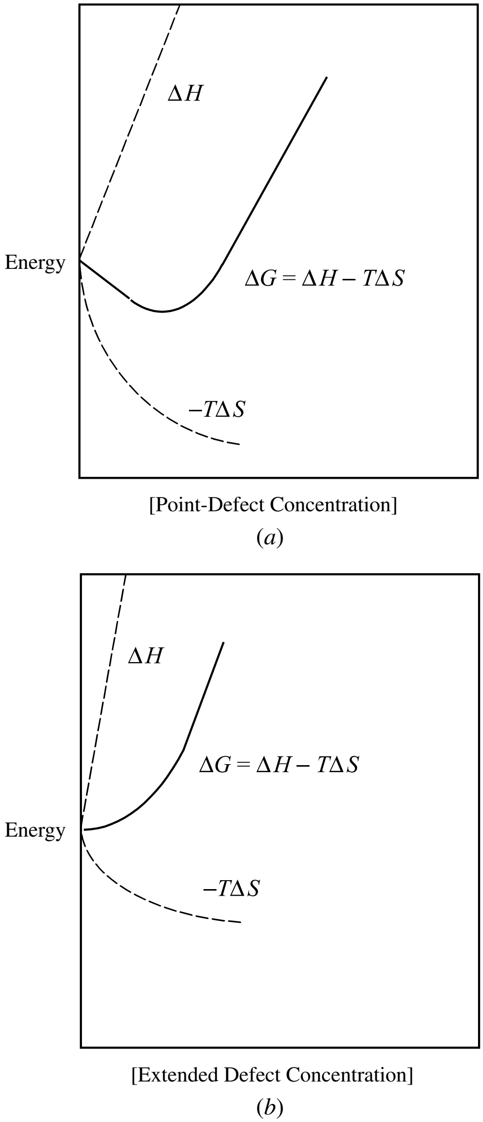

Figure 1.7 Energy changes associated with the incorporation of defects into a perfect crystal. (a) For point defects, the minimum in the free energy occurs at some finite concentration of defects. (b) For extended defects, the minimum in the free energy corresponds to the defect-free structure.

however, will raise the free energy of the system. Point defects in crystals are discussed in Sections 2.5.1 and 5.4.1.

On the other hand, the positive enthalpy of formation is so high for extended defects that the entropy gain is not sufficient to give rise to minima in the free energy (Figure 1.7b). Recall how a tilt boundary can be regarded as an array of edge dislocations. Edge dislocations are extended defects in which the formation energy must be proportional to the linear dimensions of the sample (Elliot, 1998). Hence, dislocations and grain boundaries are higher energy *metastable* configurations, introduced primarily from processing. On annealing, polycrystals tend to evolve toward single crystals through grain growth, and grains with low dislocation densities tend to grow by consuming grains with high dislocation densities.

Unfortunately, reliable grain boundary energies are hard to obtain. As one might imagine, measuring grain boundary energies is difficult and tedious. So is calculation from first principles, since this requires accurate atom positions—the determination of grain boundary structure and orientation requires careful sample preparation and high-resolution instruments. Nonetheless, some experimental work has been performed, and it is possible to make some generalized statements.

First, low Σ boundaries tend to have relatively lower grain boundary energy, on average. The entropy term is undoubtedly the dominant contribution to the free energy in these cases. With small misorientation angles ($\theta < 15°$), D in Eq. 1.10 is large. Since grain boundary energy is proportional to $1/D$, γ tends to be small for low-angle boundaries, and it has been found experimentally that as the angle exceeds 15°, the grain boundary energy typically begins to level off as it becomes independent of θ. However, one must be very cautious when attempting to correlate the three parameters, Σ, θ, and γ. Increases in Σ do often correspond to increases in θ, but not all high-angle boundaries are high Σ also. For example, the high-angle coherent twin boundary ($\theta = 60°$) is a "low sigma" $\Sigma3$ structure. Furthermore, the atoms at the interface of a high-angle coherent twin boundary are coherent, which results in a very low-energy boundary. Likewise, although many low-Σ boundaries tend to have relatively low energies, the energy does not always show a simple relationship to Σ.

1.1.5 Special Types of Low-Energy Grain Boundaries

In addition to low-energy coherent twin boundaries, other low-energy grain boundaries exist that do not involve a grain misorientation ($\theta = 0$). In a cubic close-packed (ccp) crystal, for example, the stacking repeat sequence of the close-packed layers can be represented as *...ABCABCABC...*, where each letter represents a layer of hexagonally coordinated atoms with a particular displacement relative to its adjacent layers. *Stacking faults* occur when the layer sequence is interrupted, for example, *...ABCABABC....* This type of defect commonly occurs in polytopic metals, in which the polytypes are different types of close packing. However, stacking faults can occur in non-close-packed structures as well. Figure 1.8 shows a (110) section through a diamond lattice (e.g., silicon) containing a stacking fault by removal of two adjacent layers. The diamond structure may be thought of as two interpenetrating face-centered cubic (fcc) lattices.

A second type of boundary, in which there is no misorientation between grains, is the *antiphase boundary.* This occurs when "wrong" atoms are next to each other on the boundary plane. For example, with hexagonal close-packed (hcp) crystals,

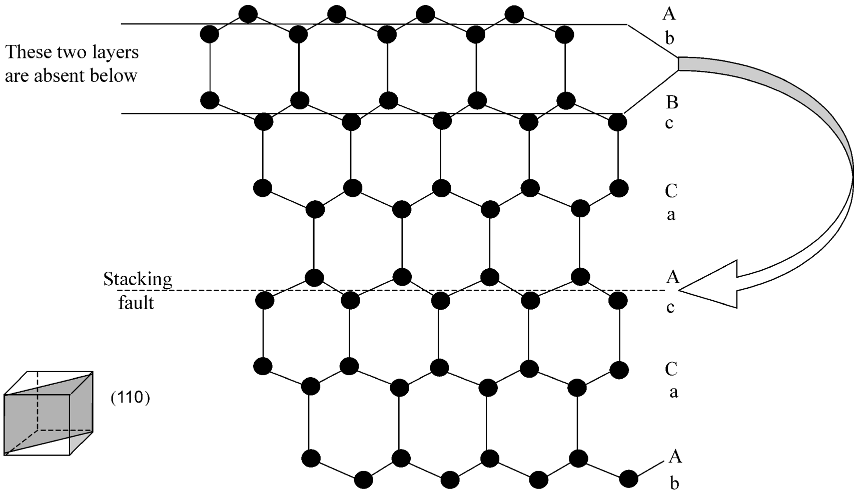

Figure 1.8 A (110) section through a diamond lattice showing a stacking fault by the absence of two adjacent atomic layers. The layer sequence along the ⟨111⟩ body-diagonal direction should be $\ldots A\ b\ B\ c\ C\ a\ A\ b\ldots$ (Adapted from Runyan and Bean, 1990, *Semiconductor Integrated Circuit Processing Technology.* Copyright © Addison-Wesley Publishing Company, Inc. Reproduced with permission.)

the sequence $\ldots ABABAB\ldots$ can be reversed at the boundary to $ABABA|ABABA$, where | represents the boundary plane. Antiphase boundaries and stacking faults are typically of very low energy, comparable to that of a coherent twin boundary.

1.1.6 Grain Boundary Dynamics

Thus far, we have confined our discussion to the "static" properties of grain boundaries. However, grain boundaries are metastable configurations and, as such, in response to external forces (e.g., thermal, mechanical) they exhibit dynamical behavior. We will briefly mention only two of the more important ones: grain boundary migration and sliding. *Grain boundary migration* is an example of when a heat-treated system attempts to minimize its free energy. Polycrystals tend to evolve toward single crystals through grain growth. In this phenomenon, atoms move from the side of the grain boundary with a high free energy to the low-energy side. The free energy of the system can thus be reduced as the low-energy crystals consume the high-energy crystals. For example, on annealing, polycrystalline grains with low dislocation densities will grow by consuming grains with high dislocation densities. Likewise, at curved boundaries atoms are more likely to diffuse from the convex side to the concave side in order to flatten the interface. In this way, the interfacial area and energy are reduced.

Grain boundary sliding is a process in which adjacent grains slide past each other along their common boundary. It is a deformation mechanism that contributes to plastic (nonrecoverable) flow and *superplasticity* in polycrystalline samples with very small grain sizes. Superplasticity has been observed in both metals and nonmetals. Superplasticity is an important property because it allows engineers to fabricate complex shapes out of a material, which might otherwise be unobtainable. Grain boundary sliding and migration modify the texture, or preferred orientation, of polycrystalline materials during recrystallization.

1.1.7 Orientation Distributions in Polycrystalline Aggregates

Methods such as high-resolution transmission electron microscopy (HRTEM) enable direct examination of orientation relationships between pairs of crystals. However, their use for the determination of preferred orientation, or *texture*, in bulk polycrystalline samples is not convenient due to the very large number of grains present. Rather, texture is normally determined from X-ray diffraction data.

In a polycrystal, the grains may all be oriented at random, exhibit some preferred orientation, or there may be multiple regions, called *domains*, possessing different preferred orientations. The most common way of illustrating texture is the use of *pole figures*. The inclination to the normal to a particular type of crystal plane [e.g., (100)], relative to some reference plane, is specified for a large number of grains. It is thus necessary to consider two coordinate systems, the *crystal coordinate system* and the *sample coordinate system*. If a sphere is imagined to enclose the polycrystalline sample, then each plane normal will intersect the sphere's surface at a point called the *pole*, which by its position on the surface represents the orientation to that crystal plane. Because it is difficult to draw a three-dimensional (3D) sphere on a 2D piece of paper, the orientation distribution is displayed with a stereographic projection of the sphere, called a pole figure. Several pole figures, one for each type of crystal plane examined, collectively describe the texture.

As an example, consider a single crystallite contained within a thin film or rolled specimen of cubic symmetry, with its (001) plane parallel to the substrate, as in Figure 1.9a. The normal to the (001) plane is pointing straight up, its $(00\bar{1})$ plane normal straight down, its (100) and $(\bar{1}00)$ plane normals pointing left and right and its (010) and $(0\bar{1}0)$ plane normals pointing front and back. Note from Figure 1.9a that the $\langle 100 \rangle$ plane normals are parallel to the sample's radial directions (RD), transverse directions (TD), and normal directions (ND). This particular arrangement is called *cube texture*.

The normal to each crystallite produces a pole by its intersection with the surface of the sphere. Hence, a large number of poles will produce a spot with a diameter that is dependent on the distance between the sample and the sphere surface. By convention, the surface of the sphere is taken to be at sufficient distance such that strong texture (a large number of parallel-plane normals) is manifested as small diameter spots. Thus, for a polycrystalline aggregate with all its crystals aligned as in Figure 1.9a the pole figure of the $\{100\}$ poles would show sharp maxima in the ND (top), RD (sides), and TD (center) locations, as illustrated in Figure 1.9b. If there were only weak cube texture, the maxima would smear out into lighter spots rather than form four distinct dark spots. This is because the plane normals are now no longer all parallel and their intersections with the sphere surface produces wide-

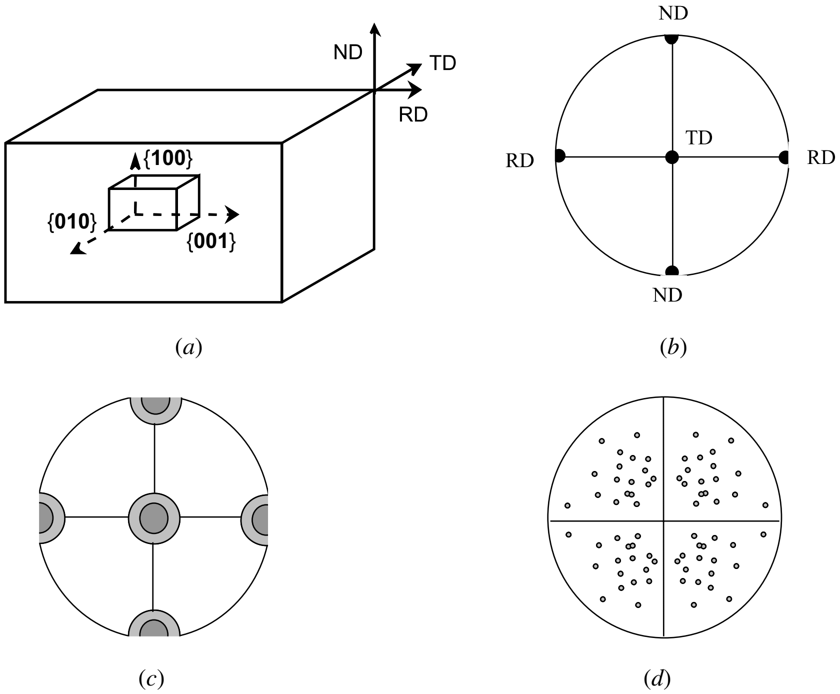

Figure 1.9 (a) Cube texture. (b) The (100) pole figure indicating sharp texture. (c) Weak texture in the (100) pole figure. (d) No preferred orientation in the (100) pole figure.

diameter less-densely populated spots, as illustrated in Figure 1.9c. If there were no preferred orientation, there would be a uniform distribution of poles in the pole figure. In this case, there is essentially one discernible pole corresponding to each crystallite whose orientation was measured, as illustrated in Figure 1.9d.

The implications of texture on the properties exhibited by a material are discussed in Sections 1.2.5, 1.3.1, and 1.3.2. We will see that the properties of polycrystalline aggregates with a sufficiently large number of grains possessing a completely random orientation distribution are macroscopically isotropic (independent of direction), even though the crystallites themselves may be anisotropic. Fabrication processes such as extrusion, rolling, and pressing, remove this isotropy, however.

1.2 SOLIDIFIED METALS AND ALLOYS

The most economical and, hence, most common method for fabricating metal pieces with a predefined size and shape is *casting*. In principle, solidification processes are equally applicable to nonmetals. However, most ceramics are very seldom prepared by this route, because of their high melting points. Typically, the molten material is poured into a thermally conducting mould to solidify. At first glance, solidification might appear to be a fundamentally simple process, but this would be deceptive. The quantitative mathematical relations governing this phenomenon are complicated moving interface diffusion equations. Fortunately, we need not present such mathematical expressions in any detail here.

In many respects, crystallization from the molten state is analogous to that from a solvent. For example, in both processes slow cooling tends to result in larger crystals, while faster cooling typically gives smaller crystals. Another important similarity involves the behavior of impurities. Impurity atoms usually do not "fit" into the crystal lattice of the solute crystallizing from a solvent. This allows crystallization from a solvent to be used as a purification technique. Likewise, impurity atoms in a polycrystalline metal tend to segregate at the grain boundaries during solidification because of their mismatch with the lattice of the metal atoms.

Conventional industrial casting processes usually involve directional heterogeneous solidification occurring in three stages: nucleus formation, crystal growth, and grain boundary formation. When enough heat is extracted, stable nuclei form in the liquid either on solid-phase impurities near the walls of the mould or on the mould itself, since this is the first region to cool sufficiently for crystals to form. Heterogeneous nucleation can also occur at the surface of the melt on solid-phase metal oxide particles. Oxides typically have much higher melting points than those of their parent metals. Other possible nucleation sites are inclusions and intentionally added grain refiners. At any rate, the solidification begins near the exterior edges and the solid–liquid interface subsequently moves inward toward the casting's center as heat is conducted through the freshly grown solid out through the mould. The nuclei consist of tiny aggregates of atoms arranged in the most favorable lattice under the process conditions. Crystals grow in all directions near the liquid–container interface. Hence, this region is called the *equiaxed zone*, as shown in Figure 1.10.

As solidification continues, an increasing number of atoms lose their kinetic energy, making the process exothermic. For a pure metal, the temperature of the melt will remain constant while the latent heat is given off (until freezing is complete). As the atoms coalesce, they may attach themselves to existing nuclei or form new nuclei. The process continues, with each crystal acquiring a random orientation and, as the gaps between crystals fill in, each grain acquires an irregular shape. The growth morphology is most likely under kinetic control, that is, the grain morphology that appears is the one with the maximum growth rate. Eventually, those grains that have a preferred growth direction will eliminate the others, resulting in the formation of a *columnar zone* where the crystals are elongated, or column-like. The growth direction is typically in the direction of heat flow. For alloys, an inner equiaxed zone can sometimes form in the casting's center, resulting from the growth of detached pieces of the columnar grains. This will be dependent on the degree of heat convection in that region.

Conventional casting procedures result in relatively coarse grains, with an average size in the range of several millimeters to several hundred micrometers. The interfaces between grains, formed by the last liquid to solidify, are the grain

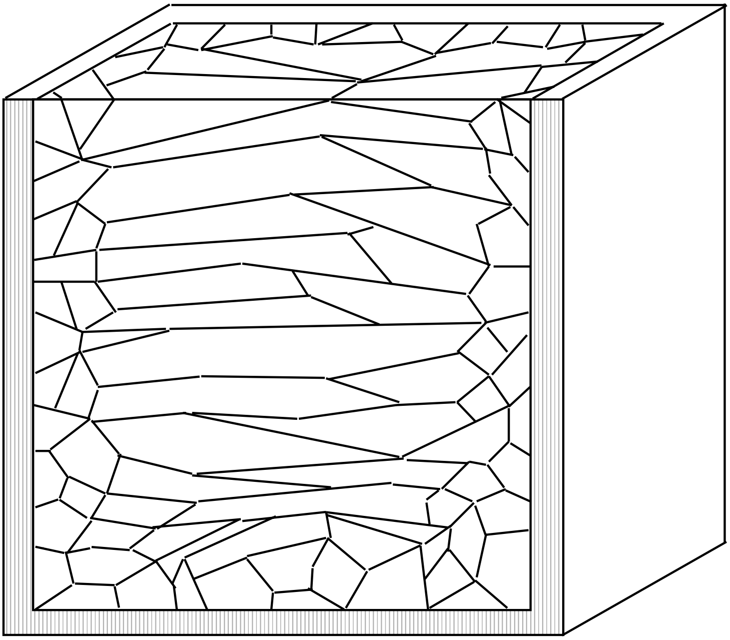

Figure 1.10 A schematic illustration of a section through an ingot showing the different solidification zones. The equiaxed zone forms near the mould walls. In the interior is the columnar zone, where crystal growth is in the direction of heat flow.

boundaries. A grain boundary is comprised of atoms that are not exactly aligned with the crystalline grains on either side of it. Hence, the grain boundaries have some degree of disorder and tend to contain a higher concentration of impurity atoms, which do not “fit” into the crystal lattices on either side of them (a melt is never *entirely* pure). The grain boundary has a slightly higher free energy due to the presence of defects. We will now investigate how grain morphology and composition, collectively termed *constitution,* is affected by the solidification rate. Of the many parameters affecting the development of the microstructure, none is more important than the cooling rate.

1.2.1 Grain Homogeneity

There are two limiting cases to consider. The first is equilibrium solidification, when the cooling rate is slow enough that solid-state diffusion can act to redistribute atoms and result in homogeneous crystals. In this case, complete diffusion occurs in both the liquid and solid. Under these conditions, the solid absorbs solute atoms from the liquid and solute atoms within the solid diffuse from the previously frozen material into subsequently deposited layers. The chemical compositions of the solid and liquid at any given temperature then follow the solidus and liquidus lines, respectively, of the equilibrium phase diagram.

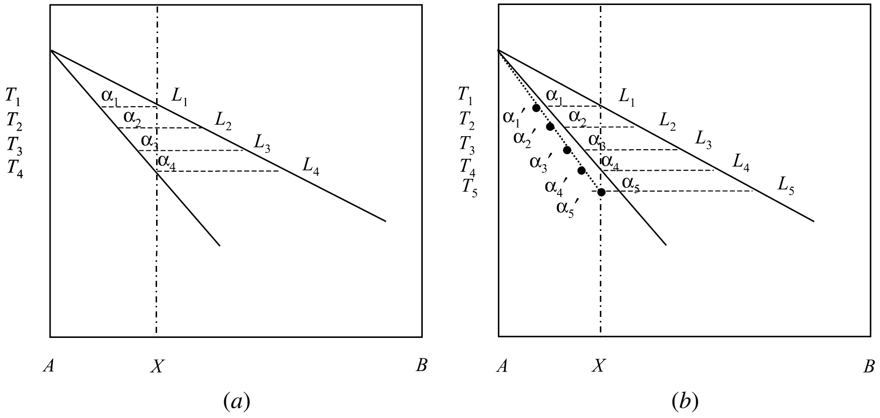

Figure 1.11 (a) A portion of a binary phase diagram illustrating equilibrium solidification. (b) Nonequilibrium (rapid) solidification, which results in a chemical composition gradient in the crystals, a condition known as coring.

Use of tie lines and the lever rule enable one to determine those compositions, as illustrated in Figure 1.11a for a binary system. The composition of the solid (C_s) as a function of the fraction solid transformed (f_s), assuming linear solidus and liquidus lines, is given by

$$C_s = kC_0/[f_s(k-1)+1] \tag{1.14}$$

where k is the partition coefficient (the ratio of the solute concentration in the solid to that in the liquid) and C_0 is the composition of the original liquid alloy. The first crystals to freeze out have composition α_1. As the temperature is reduced to T_2, the liquid composition shifts to L_2. The compositions of the freezing solid and remaining liquid continuously shift to higher B contents and leaner A contents. The average solid composition follows the solidus line to T_4, where it equals the bulk composition of the alloy.

In order to qualify for equilibrium solidification, the solidification rate must be slower than the solute diffusivity in the solid:

$$D_s \gg L_x \nu \tag{1.15}$$

where D_s is the solute diffusivity in the solid, L_x is the system length scale in one dimension, and ν is the solidification speed (Phanikumar and Chattopadhyay, 2001). Table 1.3 lists the self-diffusivities of pure metals at their freezing points (T_f) in the various structural classes. It can be deduced from Eq. 1.15 that, for a system length scale of 1 cm, the solidification rate (cm/s) must be lower than the numerical values given for the diffusivities (cm^2/s) given in Table 1.3, which are very slow rates, indeed. In other words, equilibrium solidification occurs only when the melt is cooled extremely slowly!

TABLE 1.3 Self-diffusivities for Various Metals at the Melting Temperature

Class	D_s (cm^2/s)
fcc	5.5×10^{-9}
bcc[a] (Li, Na, K, Rb)	1.4×10^{-6}
bcc (Trans. elements)	2.9×10^{-8}
hcp (Mg, Cd, Zn)	1.6×10^{-8}
Alkali halides	3.2×10^{-9}

Source: Brown, A. M.; Ashby, M. F. 1980, *Acta Met, 28*, 1085.

[a] bcc = body-centered cubic.

The second limiting case approximates conventional industrial casting processes, in which the solidification rates are several orders of magnitude too fast to maintain equilibrium. The most widely used classic treatment of nonequilibrium solidification is by Scheil (Scheil, 1942). The model assumes negligible solute diffusion in the solid phase, complete diffusion in the liquid phase, and equilibrium at the solid–liquid interface. In this case, Eq. 1.14 can be rewritten as:

$$C_s = kC_0(1 - f_s)^{k-1} \tag{1.16}$$

When the solid–liquid interface moves too fast to maintain equilibrium, it results in a chemical composition gradient within each grain (a condition known as *coring*). This is illustrated in Figure 1.11b. Without solid-state diffusion of the solute atoms in the material solidified at T_1 into the layers subsequently freezing out at T_2, the average composition of the crystals does not follow the solidus line, from α_1 to α_4, but rather follows the line α_1' to α_5', which is shifted to the left of the equilibrium solidus line. The faster the cooling rate, the greater the magnitude of the shift.

Note also that final freezing does not occur until a lower temperature, T_5 in Figure 1.11b, so that nonequilibrium solidification happens over a greater temperature range than equilibrium solidification. Because the time scale is too short for solid-state diffusion to homogenize the grains, their centers are enriched in the higher freezing component while the lowest freezing material gets segregated to the edges (recall how grain boundaries are formed from the last liquid to solidify). Grain boundary melting, *liquation*, can occur when subsequently heating such an alloy to temperatures below the equilibrium solidus line, which can have devastating consequences for metals used in structural applications.

1.2.2 Grain Morphology

In addition to controlling the compositional profile of the grains, the solidification velocity also determines the shape of the solidification front (solid–liquid interface), which, in turn, determines grain shape. The resulting structure arises from the competition between two effects. Undercooling of the liquid adjacent to the interface favors protrusions of the growing solid, which gives rise to *dendrites* with a characteristic treelike shape, while surface tension tends to restore the minimum surface configuration—a planar interface.

Consider the case of a molten pure metal cooling to its freezing point. When the temperature gradient across the interface is positive (the solid is below the freezing temperature, the interface is at the freezing temperature, and the liquid is above the freezing temperature), a planar solidification front is most stable. However, with only a very small number of impurities present in a pure melt on which nuclei can form, the bulk liquid becomes kinetically undercooled. Diffusion of the latent heat away from the solid–liquid interface via the liquid phase favors the formation of protrusions of the growing solid into the undercooled liquid (the undercooled liquid is a very effective medium for heat conduction). Ivantsov first mathematically modeled this for paraboloidal dendrites over half a century ago (Ivantsov, 1947). It is now known that this is true so long as the solidification velocity is not *too* fast. At the high velocities observed in some rapid quenching processes (e.g., $>10\ \mathrm{ms}^{-1}$), dendritic growth becomes unstable, as the perturbation wavelengths become small enough that surface tension can act to restore planarity (Hoglund et al., 1998; Mullins and Sekerka, 1963)

For a pure melt, dendritic growth is a function of the rate of latent heat removal from the interface. However, when we turn our attention to alloys, we see a slightly different situation. Here, in addition to heat flow, one must consider mass transport as well. In fact, the planar interface-destabilizing event primarily responsible for dendritic morphology in conventional alloy casting is termed *constitutional undercooling*, to distinguish it from kinetic undercooling. The kinetic undercooling contribution can still be significant in some cases. In most models for two-component melts, it is assumed that the solid–liquid interface is in local equilibrium even under nonequilibrium solidification conditions based on the concept that interfaces will equilibrate much more rapidly than bulk phases. Solute atoms thus partition into a liquid boundary layer a few micrometers thick adjacent to the interface, slightly depressing the freezing point in that region. As in the case for pure meals, the positive temperature gradient criterion for planar interface stability still holds. However, although the bulk liquid is above the freezing point, once the boundary layer becomes undercooled, there is a large driving force for solidification *ahead* of the interface into the thin boundary layer.

The critical growth velocity, ν, above which the planar interface in a two-component melt becomes unstable is related to the undercooling, ΔT_c, by an equation given by Tiller as:

$$G_L/\nu \geq \Delta T_c/D_L \tag{1.17}$$

where $\Delta T_c = m_L C_0(1 - k)/k$, and G_L is the thermal gradient in the liquid ahead of the interface, ν is the solidification speed, m_L is the liquidus slope, C_0 is the initial liquid composition, k is the partition coefficient (previously defined), and D_L is the solute diffusivity in the liquid (Tiller et al., 1953).

Constitutional undercooling is difficult to avoid except with very slow growth rates. With moderate undercooling, a cellular structure, resembling arrays of parallel prisms, results. As the undercooling grows stronger, the interface breaks down completely as anisotropies in the surface tension and crystal structure leads to side branches at the growing tip of the cells along the "easy-growth" directions ($\langle 100\rangle$ for fcc and body-centered cubic (bcc), $\langle 1010\rangle$ for hcp), marking a transition from cellular to dendritic.

Since the mid-1950s, a large amount of work has gone into obtaining accurate mathematical descriptions of dendrite morphologies as functions of the solidification and materials parameters. Dendritic growth is well understood at a basic level. However, most solidification models fail to accurately predict *exact* dendrite morphology without taking into account effects like melt flow. In the presence of gravity, density gradients due to solute partitioning produce a convective stirring in the lower undercooling range corresponding to typical conditions encountered in the solidification of industrial alloys (Huang and Glicksman, 1981). Melt flow is a very effective heat transport mechanism during dendritic growth that may result in variations in the dendrite morphology, as well as spatially varying composition (macrosegragation).

1.2.3 Microstructural Features of Multiphase Alloys

The solidification of pure metals and single-phase solid solutions has been amply discussed. It would now be beneficial to briefly describe the microstructures of multiphase alloys. The simplest type is the binary eutectic system containing no intermetallic compounds or solid-phase miscibility. An example is the Ag–Si system, the phase diagram of which is shown in Figure 1.12. At the eutectic composition (e.g., 96.9 wt% Ag in Figure 1.12), both metals form nuclei and solidify simultaneously as two separate pure phases. Generally, high-volume fractions of both phases will tend to promote lamellar structures. If one phase is present in a small-volume fraction, that phase tends to solidify as fibers. However, some eutectic growths show no regularity in the distribution of the phases. Eutectic microstructures normally exhibit small interphase spacing, and the phases tend to grow with distinctly shaped particles of one phase in a matrix of the other phase, as shown in Figure 1.13. The microstructure will be affected by the cooling rate; it is possible for a eutectic alloy to contain some dendritic morphology, especially if it is rapidly cooled.

The microstructures of *hypo*- or *hyper*eutectic compositions normally consist of large particles of the primary phase (the component that begins to freeze first) surrounded by fine eutectic structure. Often times the primary particles will show a dendritic origin, but they can transform into *idiomorphic grains* (having their own characteristic shape) reflecting the phases' crystal structure.

Multiphasic alloys sometimes contain *intermediate phases* that are atomically ordered, but that do not always crystallize in accordance with normal valency rules. Intermediate phases that exist over small compositional ranges appear as line compounds on a phase diagram. These phases are known as *intermetallic compounds*,

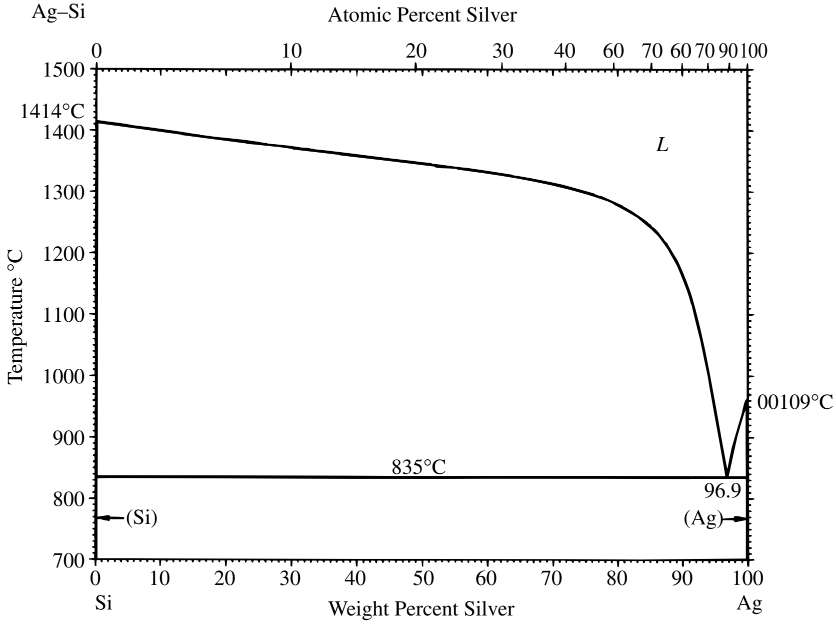

Figure 1.12 The Ag–Si phase diagram. This is the simplest type of binary eutectic system. There are no intermetallic compounds and no solid-phase miscibility. (After Baker, ed., 1992, *ASM Handbook*, Vol. 3: *Alloy Phase Diagrams*. Copyright © ASM International. Reproduced with permission.)

or IMCs (e.g., Cu_9Yb_2, Au_2Na). In contrast to the metallic bonds in a solid solution, the cohesive forces within an intermetallic may be partly covalent, ionic, or ordered metallic. Intermetallic phases are, in general, less “metallic” than metals or solid solutions. Their presence usually renders an alloy less ductile (but stronger) and lowers the thermal and electrical conductivities.

1.2.4 Metallic Glasses

It has been known for decades that in alloy systems with a deep eutectic or low-lying liquidus temperature, compared to the melting points of the pure metals, there is a strong tendency for metallic glass formation with cooling rates in the range 10^5–10^6 K s^{-1}. Such cooling rates are obtainable in industrial melt spinning and splat quenching techniques. Under these processing conditions, the highly disordered state of the supercooled liquid phase becomes “configurationally frozen” into a rigid amorphous (glassy) state. Glasses are monolithic materials, absent of grain boundaries or other crystalline defects. Some alloys can now be prepared as bulk metallic glasses (BMGs) in ribbons or rods with thickness of several centimeters, and at substantially lower cooling rates.

Glass formation can be compared to crystallization by referring to Figure 1.14, which is applicable to both metallic and nonmetallic systems. Crystallization

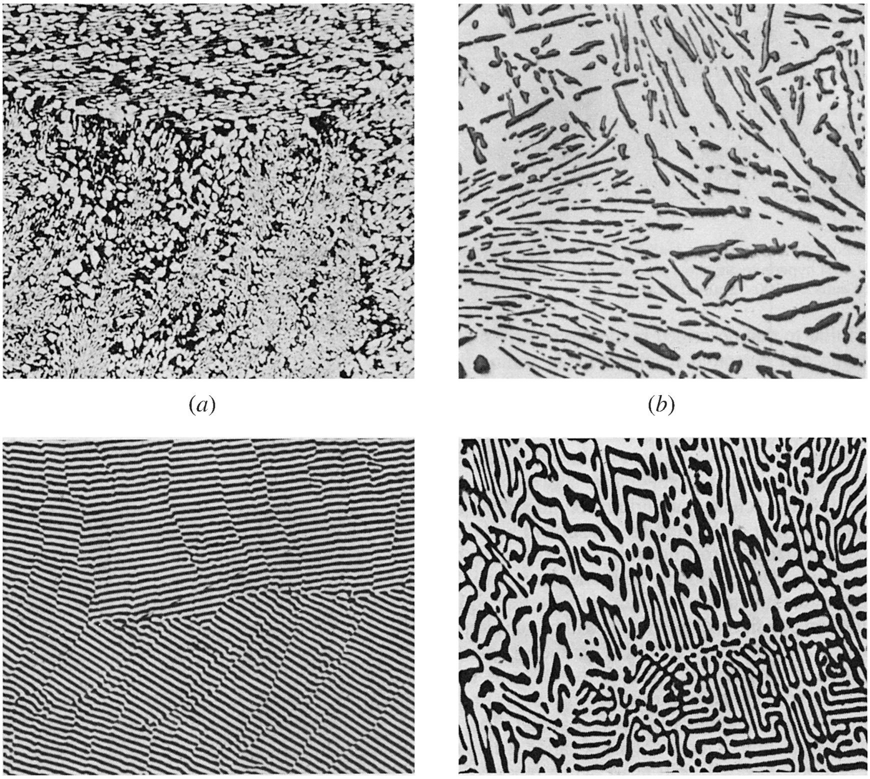

(*a*) (*b*)

(*c*) (*d*)

Figure 1.13 Various eutectic microstructures. (a) Globular (50Sn–50In). (b) Acicular (87Al–13Si). (c) Lamellar platelets (67Al–33Cu). (d) Lamellar "Chinese script" (63Mg–37Sn). (After Baker ed., 1992, *ASM Handbook*, Vol. 3: *Alloy Phase Diagrams*. Copyright © ASM International. Reproduced with permission.)

follows path *abcd*. As the temperature of a non-glass-forming melt is lowered, the molar volume of the alloy decreases continuously until it reaches the melting point, where it changes discontinuously, that is, where it experiences a *first-order* phase transition. The enthalpy and entropy behave similarly. By contrast, in glass formation the melt follows path *abef* with decreasing temperature. The liquid remains undercooled (it does not solidify) in the region *be*, below the melting point. The molar volume continuously decreases in the undercooled region and the viscosity increases rapidly. At the point T_g, called the *glass transition temperature*, the atomic arrangement becomes frozen into a rigid mass that is so viscous it behaves like a solid.

Turnbull's criterion for the ease of glass formation in supercooled melts predicts that a liquid will form a glass, if rapidly solidified, as the ratio of the glass transition temperature, T_g, to the liquidus temperature, T_l, becomes equal to or greater than 2/3 (Turnbull and Fisher, 1949; Turnbull, 1950). The T_g/T_l ratio is referred to as the reduced glass transition temperature, T_{rg}. Historically, most glass-forming alloys

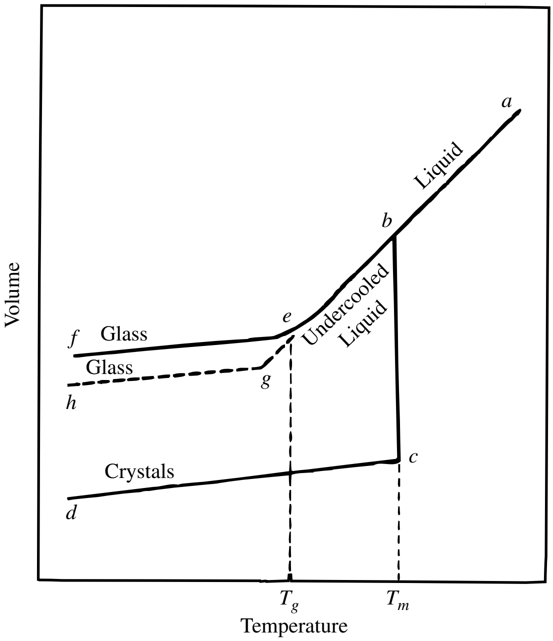

Figure 1.14 A comparison of glass formation (curve *abef*) and crystallization (curve *abcd*). The point T_g is the glass-transition temperature and T_m is the melting temperature. (After West, 1985, *Solid State Chemistry and Its Applications*. Copyright © John Wiley & Sons, Inc. Reproduced with permission.)

were metal–metalloid and metal–metal binary systems (where the metal is usually a transition element and the metalloid is B, Si, C, or P) with a T_g well above room temperature, in the range 300–700 K. With the exception of the group 12 elements (Zn, Cd, Hg) the transition metals have melting points exceeding 1200 K. Hence, those alloy systems containing very low melting eutectics (e.g., 636 K in the Au–Si system) tend to satisfy the Turnbull criterion.

Examples of binary metallic glasses include $Fe_{80}B_{20}$, $Ni_{60}Nb_{40}$, $Ni_{63}Zr27$, and $Ca_{65}Al_{35}$. The compositions of these glasses are near eutectic points (Turnbull, 1981). Turnbull's criterion has thus been validated in systems at cooling rates attainable by "conventional" casting procedures ($\sim 10^6$ K s^{-1}). Some alloy systems, such as $Cu_{60}Zr_{40}$, exhibit glass formation over composition ranges extending well beyond a eutectic point. By contrast, the T_{rg} of pure metals seem to be much smaller than 2/3. Furthermore, pure metallic liquids ($\sim 10^{-2}$ poise) have much lower viscosities than the glass-forming alloys. Therefore, glass formation from pure metal melts requires extremely high cooling rates, on the order of $\sim 10^{12}$ K s^{-1}.

There is both a kinetic and thermodynamic basis to Turnbull's criterion. The rate of homogeneous nucleation is dependent on the ease with which atomic rearrangement can occur (commonly taken as the atomic diffusion coefficient), which scales with fluidity or viscosity. Easy glass-forming substances form highly viscous melts (e.g., $>10^2$ poise), compared to non-glass-forming ones (e.g., water, with $\eta \sim 10^{-2}$ poise). In highly viscous melts, the atomic mobility is substantially reduced, which suppresses the homogeneous nucleation rate. Hence, the homogeneous nucleation rate is highly dependent on T_{rg}. The $T_{rg} > 2/3$ successfully predicts glass formation in metallic and nonmetallic liquids. Igor Evgenevich Tammann (1861–1938) pointed out, as early as 1904, that the higher the viscosity of a melt, the lower its crystallizability (Tammann, 1904). It must be noted, however, that heterogeneous nucleation (e.g., on "seed" particles) may prevent glass formation.

The preceding arguments are based on kinetics. It may also be shown on thermodynamic grounds that a high value for T_{rg} (and therefore the tendency to form a glass at lower cooling rates) is obtained for deep eutectic systems, that is, where the melting point is substantially lowered. These systems tend to be those with very little solid solubility between the components. When atoms do not "fit" together in the lattice (due to mismatches in size, valence, etc.), the tendency for crystallization diminishes. This is due to both a large negative heat of mixing and entropy of mixing for the liquid compared with the competing crystalline phase (Johnson, 2000).

Advances in metallic glasses have been made in the last couple of decades with the discovery of new families of multicomponent alloys with significantly improved glass-forming ability. Ternary glass formers include those systems in which the binary subsets exhibit limited mutual solid solubility, such as $Pd_{77.5}Cu_6Si_{6.5}$ and $Pd_{40}Ni_{40}P_{20}$. These systems have been found to form glasses at cooling rates as low as 10^3 K s^{-1} and 10 K s^{-1}, respectively. This is due to both an increased frustration of the homogeneous nucleation process and to the greater suppression of the liquidus temperature as the number of components is increased. Hence, the glass-forming ability appears to be even further enhanced in yet higher order systems, such as $Pd_{40}Cu_{30}Ni_{10}P_{20}$ (Inoue et al., 1997) and $Zr_{41.2}Ti_{13.8}Cu_{12.5}Ni_{10}Be_{22.5}$ (vitreloy 1) (Perker and Johnson, 1993). These alloys have T_g of about 582 K and 639 K, respectively, and critical cooling rates of just 1 K s^{-1}!

In the supercooled liquid state, BMGs have very high yield strength and a high elastic-strain limit (often exceeding 2%, compared with crystalline materials that are almost always less than 1%), which makes them very "springy." However, under tensile loads bulk metallic glasses lack any significant global plasticity, which limits applications as structural materials (Johnson, 1999). Recent efforts have focused on the development of engineering applications for metallic-glass containing composite materials. Such composites have been found to exhibit greatly enhanced ductility and impact resistance as compared to monolithic glasses.

Metallic glasses, like nonmetallic ones, are thermodynamically metastable states. However, metallic glasses appear to be more susceptible than nonmetallic glasses to *devitrification*, or crystallization at temperatures above T_g. They transform to more stable crystalline phases, typically around 300°–450°C. For example, nanocrystalline grains (grain size < 100 nm) can sometimes be obtained from a metallic glass when it is annealed at temperatures at which primary crystallization can occur. Nanocrystalline phases have been under increased study in recent years because they often have improved properties over their coarse-grained counterparts. Nanocrystalline alloys themselves, however, are also metastable phases, with a tendency toward grain growth.

David Turnbull (Courtesy of Materials Science Group, Division of Engineering & Applied Sciences, Harvard University © Harvard University. Reproduced with permission.)

DAVID TURNBULL

(b. 1915) earned his Ph.D. in physical chemistry from the University of Illinois at Urbana-Champaign in 1939 under T. E. Phipps. From 1939 to 1946, he was on the faculty of the Case Institute of Technology. Turnbull was a research scientist at General Electric from 1946 to 1962, as well as an adjunct professor at Rensselaer Polytechnic Institute from 1954 to 1962. He joined the faculty at Harvard University in 1962, where he was the Gordon McKay Professor of Applied Physics, becoming emeritus in 1985. Turnbull was a pioneer in the study of kinetic phenomena in condensed matter. He performed the critical experiment in several areas: nucleation and growth of crystals; diffusion in crystalline and amorphous materials; and viscous flow of amorphous materials. He formulated the classic theory for nucleation in condensed matter and, with Morrel Cohen, the free volume theory for the flow of liquids and glasses. He predicted that glass formation is universal, anticipated the discovery of metallic glasses, and demonstrated the first formation of metallic glasses in bulk form. The Turnbull criterion predicts the ease with which glass formation occurs. Turnbull was awarded the von Hippel Prize of the Materials Research Society, the Acta Metallurgica Gold Medal in 1979, and the Japan Prize in 1986. The Materials Research Society named an annual lecture after him. He was elected to the U.S. National Academy of Sciences in 1968.

(*Source*: B. Sewall and F. Spaepen, personal communication, February 25, 2004.)

1.2.5 Microstructure/Property Correlation and Control in Metals

Mechanical properties are studied in detail in Chapter 9. Here, we present a brief introduction appropriate for the present discussion. The microstructures of all metals and alloys greatly influence strength, hardness, malleability, and ductility. These properties describe a body's *plasticity*, or ability to withstand permanent deformation without rupture. Plastic deformation is due to the gliding motion, or *slip*, of planes of atoms. Slip most readily occurs on close-packed planes of high atomic density in the close-packed directions. However, much smaller stresses are required to move a dislocation through a crystal than a full plane of atoms. Therefore, dislocations actually govern the ability of a coarse-grained material to plastically deform. Dislocations have already been introduced. One type is the edge dislocation, which is an extra half-plane of atoms.

Polycrystalline materials are stronger than single crystals. It is not easy for dislocations to move across grain boundaries because of changes in the direction of the slip planes. Thus, the mechanical properties of polycrystalline metals are dependent on the average grain size and the orientation distribution, or *texture*. Deformation processes such as rolling and extrusion, which rely on plasticity, introduce texture into a sample. The *elasticity* of a polycrystal, or ability of the body to return to its original size and shape upon removal of a mechanical stress, is also a function of texture. Strictly speaking, this is true so long as the following conditions are met: (1) the number of grains in the sample is sufficiently large; (2) there is no preferred orientation; (3) the polycrystal is under homogenous strain and stress (i.e., all grains experience the same strain and stress); and (4) grain boundaries do not contribute to the body's elasticity.

Other physical properties of polycrystalline metals, such as electrical and thermal conduction, are also affected by microstructure. Point defects (vacancies, impurities) and extended defects scatter electrons and phonons, shortening their mean free paths. An approximation known as *Matthiessen's rule*, from the nineteenth-century physicist Ludwig Matthiessen (1830–1906), asserts that all the various scattering processes are independent (strictly true only so long as the scattering processes are isotropic). Hence, the contributions to the resistivity can simply be added up. The electrical resistivity of a polycrystalline metal is then the sum of the contributions due to electron scattering in the bulk crystal and at the interfaces, the latter of which is a function of the grain boundary structure. Furthermore, the resistivity of a fine-grained metal is higher than that of a coarse-grained sample because the former has a larger number of grain boundaries.

Transport properties are second-rank tensors, which are only isotropic for cubic crystals and polycrystalline aggregates with a random crystallite orientation. For all other cases, the conductivity will be dependent on direction. A noncubic polycrystalline metal or alloy will show a texture dependency. However, because most metals are in the cubic class, we postpone a discussion of this topic until Section 1.3.1 on the transport properties of ceramics, where the effect is more marked.

In addition to specifying the texture or orientation distribution to the grains (Section 1.1.7), we can specify the fraction of a particular CSL boundary type

(Section 1.1.3). This approach is also useful because the grain boundary structure often correlates with certain materials properties, particularly conductivity, creep (time-dependent deformation at constant load), and corrosion. The incorporation of a high percentage of a specific grain boundary type in a polycrystal is referred to as *grain boundary engineering*. For example, coherent twin boundaries are able to block dislocation motion and strengthen a metal. They also allow for a much more efficient transfer of current than do conventional grain boundaries. Hence, metals with a high percentage of coherent twin boundaries are strengthened without a loss to the electrical conductivity. Likewise, it has been shown that Ni–Cr–Fe alloys with a high fraction of special CSL boundaries possess higher creep resistances (lower strain rates) than those with general boundaries (Thaveepringsriporn and Was, 1997; Was et al., 1998).

Grain boundary structure also contributes to the chemical properties exhibited by a metal. *Inter*granular atomic diffusion processes occur more rapidly than *intra*-granular ones, since these regions are usually not as dense as the grains. Remember also that grain boundaries have a higher free energy than the grains themselves. Because of these aspects, a metal will usually oxidize or corrode more quickly at the grain boundaries, a condition known as intergranular corrosion. The oxidation rate may be very dependent on the grain boundary structure. Again, this gives rise to the possibility for grain boundary engineering. For example, it has been shown that Ni–Fe (Yamaura et al., 2000) alloys and Pb electrodes (Palumbo et al., 1998) deformation processed or thermally processed to have a high fraction of low-Σ boundaries are much more resistant to intergranular corrosion, while those with random high-angle boundaries, which are probably higher in energy, more easily oxidize. For conventionally grained solids, however, the grain boundary volume is a small fraction of the total volume of the sample. Hence, intragranular diffusion is usually the dominant mass-transport process, except for very small grain sizes or at low temperatures. Nonetheless, because impurity atoms tend to segregate at grain boundaries, intergranular chemical reactions that may not occur intragranularly are possible.

Materials processing is generally aimed at achieving a texture and/or grain boundary structure that will maximize a specific property of interest. Approaches with polycrystalline metals and alloys usually involve deformation processing and annealing, or a combination thermomechanical method. During fabrication processes, such as cold rolling, for example, polycrystalline metals deform by mechanisms involving slip and, where slip is restricted, *rotation* of the individual grains. Both processes, of course, must satisfy the condition that the interfaces along which the grains are connected remain intact during deformation. As the extent of deformation increases, larger grains may break up into smaller grains of different orientations, giving rise to an orientation spread. Similar changes accompany both hot working and annealing. In these procedures, the free energy of a metal decreases due to rearrangement of dislocations into lower energy configurations of decreased dislocation density. This is termed *recovery*. However, in competition with this is *recrystallization*, in which the resulting grain structure and texture depend on the spatial distribution and orientation of the recrystallization nuclei. The competition between these two processes and their effect on texture and grain boundary structure is a hotly debated subject in metallurgy.

1.3 CERAMIC POWDER AGGREGATES

Traditionally, ceramics have been defined rather broadly as all man-made inorganic nonmolecular materials, excluding metals and semiconductors. Solidification processes, like those discussed in the previous section, are very seldom used to prepare ceramics. This is because ceramics normally have exceedingly high melting points, decompose, or react with most crucible materials at their melting temperatures. In the past, ceramics were prepared only by high-temperature solid-state reactions, which came to be known as the *ceramic* method. This restriction was lifted to a certain degree with the advent of lower temperature (up to a few hundred degrees) soft chemical routes, such as ion exchange, intercalation, and topochemical reactions, where the reactivity is controlled by the crystal structure of the starting material.

The products of most ceramic syntheses are powders. Fabricating a bulk part from a powder requires a forming process, usually compaction (either compression molding or injection molding) followed by sintering. The latter step involves heating the phase at a temperature below its solidus (melting point), but high enough that grain growth occurs via solid-state diffusion. In the early stages of sintering, volatile species can be removed (e.g., moisture content) and, at later stages, homogenization improved (e.g., the removal of macrosegragation), and densification increased as the particles bond together, eliminating pores. The resultant products have higher strength and reliability.

1.3.1 Transport Properties of Polycrystalline Ceramics

Although polycrystals are mechanically superior to single crystals, they have inferior transport properties. Quite a large number of ceramics are actually electrical conductors, that is, they exhibit a metallic-like conductivity. However, a polycrystal has a lower thermal and electrical conductivity than a single crystal because of phonon and electron scattering at grain boundaries. Generally, the smaller the grain size, the larger the total interfacial volume and the lower the conductivity. We will see a specific example of this grain-size dependence later in Section 7.4.2 of Chapter 7. In addition to this effect, it is also important to understand the effect of texture on transport properties. The conductivities of all crystal classes other than the cubic class are anisotropic, or dependent on direction. Some ceramics are even low-dimensional transport systems, in which conduction is much weaker or completely absent along one or more of the principal crystallographic axes. If the transport properties of the individual crystallites in a polycrystalline aggregate are anisotropic, such as in a low-dimensional system, sample texture will influence the anisotropy to the conductivity of the polycrystal.

When a polycrystal is free of preferred orientation, its transport properties will be, like a cubic crystal, macroscopically isotropic regardless of the anisotropy to a

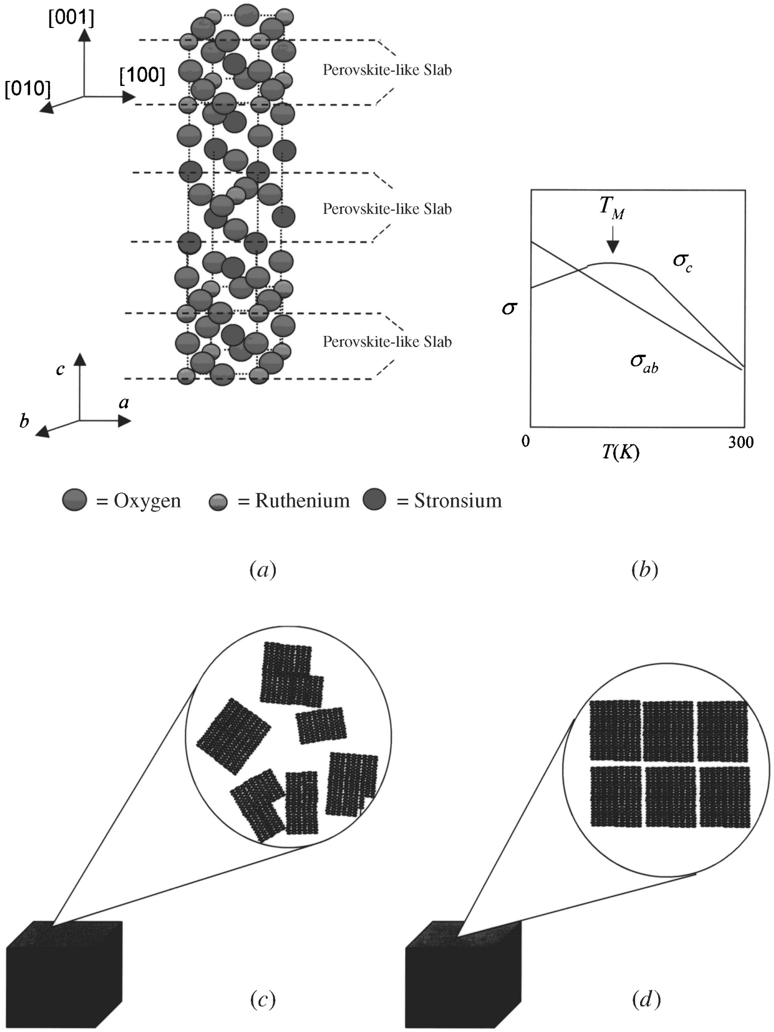

(*a*) (*b*)

(*c*) (*d*)

Figure 1.15 (a) The crystal structure of Sr_2RuO_4. (b) Above T_M, conduction in the *ab* planes within the perovskite layers is metallic, while the *c*-axis transport is semiconducting. (c) Random orientation in a powder aggregate with different crystallite sizes. Percolation paths exist for both σ_{ab} and σ_c in all directions, resulting in an isotropic conductivity at any given temperature. (d) If identical crystallites are all aligned with their *c* axes parallel, the polycrystal will have the same anisotropic conductivity as a single crystal.

single crystallite. For example, consider the low-dimensional metal Sr_2RuO_4, with the tetragonal crystal structure shown in Figure 1.15a. At high temperatures, metallic conduction occurs in the *ab* planes within the perovskite layers, parallel to the two principal axes $\langle 010 \rangle$ and $\langle 100 \rangle$. Transport along the *c*-axis, perpendicular to the *ab* plane, is semiconducting at high temperatures.

For polycrystals, two extreme orientation distribution functions, which give the volume fraction $f(x)$ of crystals in orientation x, can be envisioned. These are zero preferred orientation or perfect alignment. The absence of preferred orientation statistically *averages* out the parallel and perpendicular conduction effects in Sr_2RuO_4. The bidimensional metallic conductivity, which is clearly observed in a single crystal, is completely inhibited in free powders composed of millions or billions of randomly oriented crystallites. This is shown in Figure 1.15c. By contrast, we can expect the application of several thousand pounds of uniaxial pressure in forming a pellet (i.e., a cylindrical shaped specimen) to induce a high degree of texture. This is especially true for elongated platelet crystals, where the c axes of the crystallites align parallel to the pressure axis. We cannot assume that all the crystals are identical in size and shape. Thus, with the application of uniaxial pressure alone many crystallites will remain misoriented. Higher degrees of texture may sometimes be induced by magnetic fields because of the anisotropy to the magnetic susceptibility (Section 1.3.4).

If the Sr_2RuO_4 crystallites were to be identical and perfectly aligned with their c axes parallel (somewhat like stacking children's building blocks), the pellet's resistivity would exhibit the same anisotropy as a tetragonal single crystal of Sr_2RuO_4. The resistivity along the *ab* axis of the pellet would follow the ρ_{ab} curve in Figure 1.15b, while the resistivity along the c-axis would follow the ρ_c curve. This is illustrated in Figure 1.15d. Nonetheless, the current density of the pellet would be lower than that of a single crystal of the same dimensions due to the grain boundary resistance.

We can gain further enlightenment on electrical conduction in polycrystals by likening the phenomenon to a random resister network with the *bond percolation model*. In this model, we have a lattice, where each site corresponds to an individual crystallite of the polycrystalline aggregate. We make the simplifying assumption for now that all sites, or crystallites, are equivalent electrical conductors. The grain boundaries are the "bonds" connecting the individual lattice sites. Each grain boundary has an electrical resistance, R_{GB}, that is dependent on the orientation relationships of the grains. For now, let us also assume a bimodal R_{GB}, that is, that 0 (superconducting) or ∞ (nonconducting) are the only two possible values for R_{GB}. Each bond is either "open" with probability p, or "closed" with probability $(1-p)$. The open bonds allow passage of current and the closed bonds do not.

The main concept of the bond percolation model is the existence of a percolation threshold, p_c, corresponding to the point at which a cluster of open bonds (a conducting path) first extends across the entire sample. Such a cluster is called a *spanning cluster*. For all $p < p_c$, no current can flow due to the lack of a complete current path, but there may be nonspanning clusters, connecting a finite number of points, which exist for any nonzero p. At p_c, the system abruptly transitions to the electrically conductive state, and for all $p > p_c$, the sample is electrically conducting because of the presence of spanning clusters.

For $p > p_c$, the conductivity, σ, is proportional to a power of $(p-p_c)$:

$$\sigma \propto (p-p_c)^{\mu} \tag{1.18}$$

The exponent μ is called a scaling exponent. It depends on the dimensionality of the system. For 2D transport, $\mu = 1.30$ and for 3D transport, $\mu = 2.0$ (Stauffer and Aharony, 1994).

The numerical value of the bond percolation threshold is dependent on the geometry of the grain boundary network. For example, p_c is equal to 0.500 for a simple 2D square lattice and 0.388 for a 3D diamond lattice. For the simple cubic, fcc, and bcc lattices, p_c is equal to 0.2488, 0.1803, and 0.119, respectively. With nontextured polycrystals, the geometries (grain orientations and/or angles) are random, and hence, the exact value for p_c may not be known. Furthermore, our original assumption that the grain boundaries are either superconducting or insulating is obviously a drastic one. In reality, the grain boundary resistance is not bimodal. It can have values other than zero or infinity, which are dependent on the grain orientations and/or angles, as can be inferred from Figure 1.15c. In fact, a broad distribution of grain boundary resistances may be observed. For sufficiently broad distributions, however, the resistance of the bulk sample is often close to the resistance of the grain boundary cluster with exactly the percolation threshold concentration (Stauffer and Aharony, 1994). For a derivation of Eq. 1.18, as well as a detailed treatment of percolation theory, the interested reader is referred to the book by Stauffer and Aharony (1994).

Example 1.3 The oxide $Bi_4V_2O_{11}$ is similar in structure to the layered Aurivillius phase Bi_2MoO_6 (tetragonal crystal class). The aliovalent exchange of Mo^{6+} by V^{5+} results in oxygen vacancies in the BiO_6 octahedral layers, which are separated along the *c*-axis by edge-sharing BiO_4 pyramids. The oxygen-ion conduction in $Bi_4V_2O_{11}$ is highly bidimensional, being much stronger in the *ab* planes of the octahedral layers than in the perpendicular out-of-plane direction along the *c*-axis. Speculate on what the (001) pole figures for each sample given in Table 1.4 would look like.

Solution The (001) pole figure for the single crystal must have a single spot in the middle of the circle since all (001) planes in a single crystal are parallel. The anisotropy in the conductivity would be expected to be the greatest. The (001) pole figure for the pressed polycrystal should show the greatest spread, or orientation distribution, to the grains. This is because the anisotropy to the conductivity of the

TABLE 1.4 Sample of (001) Pole Figures[a]

	$\sigma_{\|}$	σ_{-}
Single crystal	73.2	2.6
Pressed polycrystal	40.2	20.2
Magnetically aligned polycrystal	59.1	13.8

Source: The data are from Muller, C.; Chateigner, D.; Anne, M.; Bacmann, M.; Fouletier, J.; de Rango, P. 1996, *J. Phys. D*, *29.*

[a] Conductivities ($\times 10^3$ S cm^{-1}).

polycrystal was observed to be the smallest. Its properties are closest to that of a randomly textured sample. The (001) pole figure for the magnetically aligned polycrystal should have an intermediate spread since its anisotropy to the conductivity was intermediate.

1.3.2 Magnetic and Dielectric Properties of Polycrystalline Ceramics

Just as crystals can have an easy direction for the transport of charge carriers, they will likewise magnetize along easy axes of magnetization. The interactions between subgrain domains of ferromagnetic and ferroelectric polycrystals further complicate behavior. Subgrain domains form because the energy density associated with the magnetic flux density exerted outside a sample is decreased if domains with opposing magnetizations are created (Elliot, 1998). In the absence of an external field, each domain exhibits spontaneous magnetization, or polarization in the case of ferroelectrics, which can be represented by the resultant net vector for that domain. However, a macroscopic crystal generally will exhibit very little magnetization in zero fields. This is because the individual domains have their vectors pointing in different directions, giving rise to a zero net magnetization or polarization. In the presence of a sufficiently strong applied field, saturation is reached, where the dipoles in all the domains within the crystal align.

Polycrystalline materials possess a texture, or orientation distribution to the grains, and each grain may contain several domains (see Figure 1.16). We might therefore expect that neighboring grains, and the domains within them, would interact magnetically in very different ways, giving rise to a response that will be very dependent on the grain size and texture. Such behavior is expected in the plots of magnetization versus applied field, so-called *hysteresis* loops, that follow one

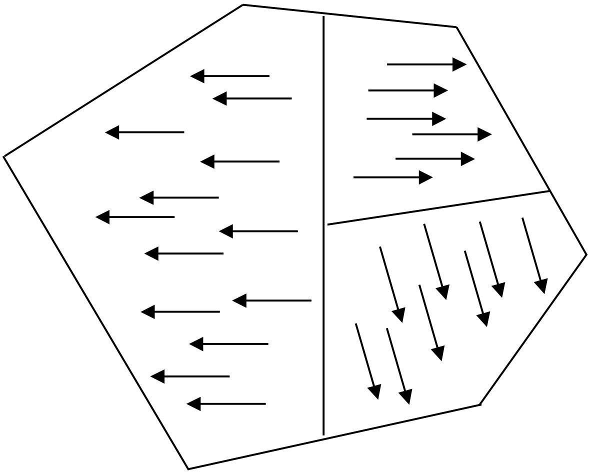

Figure 1.16 Schematic drawing of subgrain magnetic domains. Each of the three domains shown has a different net magnetic moment.

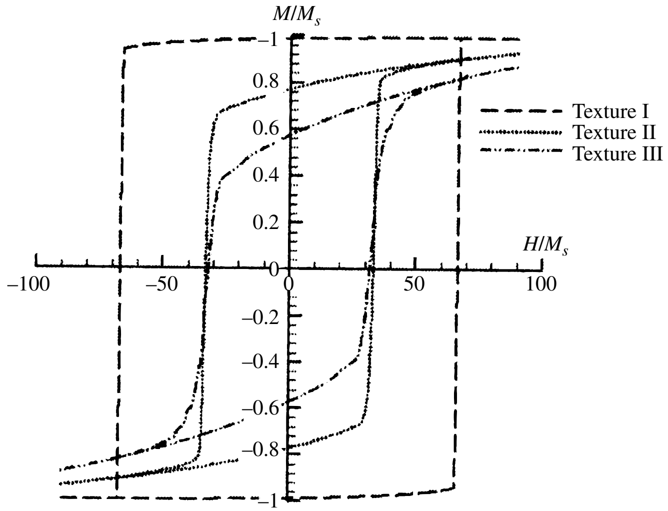

Figure 1.17 Simulated hysteresis loops for polycrystalline films with different textures. (After Jin et al. 2002, *J. App. Phys.*, *92*, 6172. Copyright © American Institute of Physics. Reproduced with permission.)

complete cycle of magnetization and demagnetization in an alternating field. Simulated hysteresis loops for polycrystalline films with different textures are shown in Figure 1.17. The greater the misalignment among grains, the less the magnetization that remains after the field is removed (*remanence*), and the lower the magnitude of the reverse field required for demagnetization (*coercivity*) (Jin et al., 2002). If these parameters can be controlled by manipulating the microstructure, different magnetic properties can be designed. For example, if ultrasmall (i.e., nanosized) grains of a highly magnetocrystalline–anisotropic thin-film material can be deposited with all their easy magnetization axes normal to the film, magnetic storage media with much greater recording densities can be obtained.

1.3.3 Mechanical Properties of Ceramics

The mechanical properties of ceramics differ greatly from those of metals. Ceramics are typically brittle, very strong, hard, and resistant to deformation. It is found that dislocation motion is virtually impossible except at high temperatures. In ionic solids, slip is constrained because it requires bringing ions with like charges in contact. Furthermore, although many ionic solids are "almost" close packed, slip is very difficult on anything but truly close-packed planes. The strong and directional bonding present in covalent solids similarly impedes dislocation motion since it requires bond breaking and distortion.

The absence of a lattice-based mechanism, such as slip planes, does not necessarily preclude all deformation. Plastic flow can proceed in other modes. For example, at temperatures of about 40–50% of their melting points, grain boundary sliding can become important. Grain boundary sliding is believed to be the major contributor to the superplasticty observed in some polycrystalline ceramics.

1.3.4 Texture Control in Ceramics

We have already mentioned that one method of producing a textured ceramic involves the application of uniaxial pressure to form a cylindrical-shaped specimen. However, in this method, there usually remain a large number of misoriented grains. Furthermore, this simple approach is not applicable for every desired shape. There are other methods that have been used to produce textured ceramics. One is the templated grain growth (TGG) method, in which anisotropic seed particles regulate crystal growth in specific growth directions. This process involves the addition of a small amount of the template particles (usually less than 10 vol %) that is, seed particles of the same substance, to a powder matrix. The template particles are next oriented and the matrix is then sintered, causing the template particles to grow by consuming the randomly oriented matrix. This produces a highly oriented microstructure.

When the unit cell of a crystalline ceramic substance is anisotropic, this gives rise to the possibility that the accompanying anisotropy in its physical properties may aid the texture control of powder samples. For example, a crystal with an anisotropic magnetic susceptibility will rotate to an angle, minimizing the system energy when placed in a magnetic field. The reduction in magnetic energy is the driving force for magnetic alignment. However, alignment may be difficult in nondispersed powders because of strong particle–particle interactions that prevent the particles from moving. Therefore, dispersion of the powder in a suspension is usually necessary for effective utilization of a magnetic field. This can be readily accomplished in *slip casting*, where a suspension, or slurry, called the *slip*, is poured into a porous mold of the desired shape that absorbs the fluid. Magnetic alignment, in conjunction with slip casting, has been used to produce textured microstructures in a variety of substances, including some with only small anisotropic diamagnetic susceptibility, such as ZnO and TiO_2, if the magnetic field is high enough (e.g., several tesla).

1.4 THIN-FILM MICROSTRUCTURE

The cornerstone of the entire semiconductor microelectronics industry is thin-film technology. There are many methods available for growing thin films, including physical vapor deposition (PVD) (e.g., sputtering, evaporation, laser ablation); chemical vapor deposition (CVD); plating; and so-called soft chemical techniques (e.g., sol-gel coating). Most of these processes are well established in the microelectronics industry, but many also have important applications in the areas of advanced coatings and structural materials. An enormous variety of films can be prepared. The interested reader is encouraged to refer to any of numerous texts on thin films for details regarding the deposition processes.

An exciting new area of materials research that has begun to evolve in recent years is the application of combinatorial chemistry to the creation of thin-film libraries. By using masks (grids with separate squares), thousands of distinct combinations of materials can, in principle, be deposited onto a single substrate in order to greatly accelerate the screening of the resultant compounds for certain properties. This is part of a broad approach being sought for the rapid discovery of new materials known as *combinatorial materials science*, inspired by the success of combinatorial chemistry in revolutionizing the pharmaceutical industry.

1.4.1 Epitaxy

Thin films can be polycrystalline or single crystalline. The majority of thin films are polycrystalline. Single crystal films can be grown with a particular crystallographic orientation, relative to a single-crystal substrate that has a similar crystal structure, if the deposition conditions and substrate are very stringently selected. *Homoepitaxy* refers to the growth of a thin film of the same material as the substrate (e.g., silicon on silicon). In this case, the crystallographic orientation of the film will be identical to that of the substrate. In *heteroepitaxy*, such as silicon on sapphire, the layer's orientation may be different from that of the substrate. Both types of epitaxy often proceed by an island nucleation and growth mechanism referred to as Volmer–Weber growth.

Island growth also occurs with polycrystalline films, but in epitaxy, the islands combine to form a continuous single-crystal film, that is, one with no grain boundaries. In reality, nucleation is much more complex in the case of heteroepitaxy. Nucleation errors may result in relatively large areas, or domains**,** with different crystallographic orientations. The interfaces between domains are regions of structural mismatch called *subgrain* boundaries and will be visible in the microstructure.

Epitaxy has been used to stabilize films with crystal structures that are metastable in the bulk phases. Kinetic stabilization is obtained when the growth is performed under conditions of high surface diffusion, but low bulk diffusion. In this way, crystallographically oriented film growth occurs, while phase transformations are prohibited. The circumstances under which thermodynamic stabilization can be achieved have also been enumerated. Namely, by minimizing: (1) the lattice mismatch, or structural incoherency, and the free-energy difference between the growing film and the substrate; (2) the film thickness; and (3) the shear and elastic moduli of the film. Additionally, the growing film should be able to form a periodic multiple-domain structure (Gorbenko et al., 2002).

The high-temperature bulk fcc phase δ-Bi_2O_3 is observed on heating α-Bi_2O_3 (monoclinic structure) above 717°C, but heteroepitaxial thin films of δ-Bi_2O_3 have been deposited on an fcc gold substrate at temperatures as low 65°C. Similarly, $YMnO_3$ crystallizes in the hexagonal structure under atmospheric pressure at high temperatures, yet was grown by pulsed laser deposition (PLD) as a stable perovskite film on an $NdGaO_3$ substrate (Salvador et al., 1998). It has also recently been shown how metal–organic chemical vapor deposition (MOCVD) results in the formation of metastable phases of GaS and GaTe, irrespective of the structure of the substrate (Keys et al., 1999; Gillan and Barron, 1997). Crystalline GaS was even grown on an amorphous substrate. It appears in these cases that the precursor's structure or its decomposition mechanism completely controls the structure of the thin film. Likewise, polycrystalline CVD diamond is commercially grown on a variety of substrates, including titanium, tungsten, molybdenum, SiO_2, and Si_3N_4. Each of these materials is capable of forming a carbide layer upon which an adherent diamond film can nucleate, although it is not clear whether carbide formation is essential.

1.4.2 Polycrystalline PVD Thin Films

The commonest morphology exhibited by PVD thin films is the highly oriented columnar (fiber) grain growth shown in Figure 1.18. This is a consequence of the fact that PVD processes generally deposit thin films atom by atom in a "line of site" fashion wherein the sputtered or evaporant *adatoms* travel from the source to substrate on a straight path. The resulting grains are thus aligned with their long axes perpendicular to the surface when the incident beam arrives at a normal angle of incidence. If the depositing atoms arrive at an angle away from normal incidence, the columns tilt into the oncoming beam. This gives rise to shadowing effects, which result in the columns separated from one another by voids. In either case, the grains can completely traverse the thickness of the film. Sputtered films generally tend to be denser, more amorphous in nature, and more adherent than evaporated films because of the higher energy of the arriving adatoms.

Slight variations can occur with columnar morphology, however. For example, Movchan and Thornton used structure zone models to illustrate how temperature influences the morphology of metal films (Movchan and Demchishin, 1969; Thornton, 1977). Grain growth often begins with island formation (nucleation sites). When the homologous temperature, T_h (for thin films this is the ratio of the substrate temperature to the melting point of the thin film), is <0.3, the surface mobility of the deposited atoms, or adatoms, is low. As the homologous

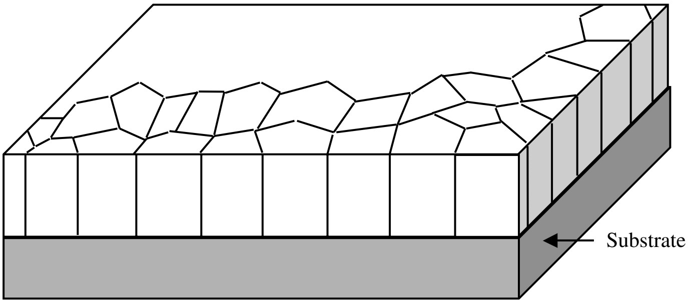

Figure 1.18 Highly oriented columnar (fiber) thin film. The grains are oriented with a preferred crystal direction normal to the substrate along the growth axis, but with no orientation relationship about the growth axis.

temperature increases ($0.3 < T_h < 0.5$), the surface mobility increases. Thus, the islands may initially evolve three-dimensionally into V-shaped columns. Once the V-shaped columns impinge on one another, the grain boundaries become parallel and a dense structure is obtained. Finally, when $T_h > 0.5$, bulk diffusion increases substantially and allows for equiaxed grains. A major disadvantage of PVD thin films is its inability for conformal coating, that is, it produces poor step coverage. Residual stresses in PVD thin films are generally compressive.

As with solidification microstructures, kinetic factors are as important as thermodynamics. For example, the (200) surface has the lowest energy in TiN. But the preferred orientation of TiN thin films can vary between (111) and (200), depending on deposition conditions. This means that the texture depends on kinetic factors as well as the energy minimization.

1.4.3 Polycrystalline CVD Thin Films

Chemical-vapor deposition is a process in which a volatile species is transported in the vapor phase to the substrate to be coated. Typically, a chemical reduction then occurs at the substrate to deposit the desired film. For example, volatile $ReCl_5$ will deposit rhenium on a substrate heated to 1200°C. Although adatom energy exerts the strongest influence on film morphology in PVD processes, CVD is dominated by chemical reaction kinetics. The islands grown in CVD processes tend to be larger in size and fewer in number. There also appears to be marked temperature dependence to the growth rate. Kinetic Monte-Carlo (MC) simulations have shown that grain morphology in CVD thin films is primarily due to an autocatalytic process, in which precursor molecules dissociate preferentially at existing nuclei sites (Mayer et al., 1994). Another difference between PVD and CVD films is that, in PVD, the residual stress in the deposited film is normally compressive, whereas in CVD, it is generally tensile. Nevertheless, as with PVD, the most common microstructure produced from CVD is the highly oriented columnar structure.

REFERENCES

Aust, K. T.; Rutter, J. W. 1959, *Trans. AIME*, *215*, 119.

Bhadeshia, H. K. D. H. 1987, *Worked Examples in the Geometry of Crystals*, The Institute of Metals, London, p. 70.

Bollman, W. 1967, *Phil. Mag.*, *16*, 363.

Bollman, W. 1970, *Crystal Defects and Crystalline Interfaces*, Springer-Verlag, Berlin.

Brandon, D. G.; Ralph, B.; Ranganathan, S.; Wald, M. S. 1964, *Acta Metall.*, *12*, 813.

Chen, F.-R.; King, A. H. 1988, *Acta Crystallogr. B*, *43*, 416.

Elliot, S. R. 1998, *The Physics and Chemistry of Solids*, John Wiley & Sons, Chichester, UK.

Friedel, G. 1926, *Lecons de Cristallographie*, Berger-Levrault, Paris.

Gillan, E. G.; Barron, A. R. 1997, *Chem. Mater.*, *9*, 3037.

Gorbenko, O. Y.; Samoilenkov, S. V.; Graboy, I. E.; Kaul, A. R. 2002, *Chem. Mater.*, *14*, 4026.

Hargreaves, F. Hill, R. T. 1929, *J. Inst. Metals*, *41*, 237.

Hoglund, D. E.; Thompson, M. O.; Aziz, M. J. 1998, *Phys. Rev. B*, *58*, 189.

Huang, S. C; Glicksman, M. E. 1981, *Acta Metall.*, *29*, 71.

Inoue, A.; Nishiyama, N.; Kimura, H. 1997, *Mater. Trans. JIM*, *38*, 179.

Ivantsov, G. P. 1947, *Dokl. Akad. Nauk*, *58*, 56.

Jin, Y. M.; Wang, Y. U.; Kazaryan, A.; Wang, Y.; Laughlin, D. E.; Khachaturyan, A. G. 2002, *J. App. Phys.*, *92*, 6172.

Keys, A.; Bott, S. G.; Barron, A. R. 1999, *Chem. Mater.*, *11*, 3578.

Johnson, W. L. 2000. In: Turchi, P. E. A., Shull, R. D., editors, *The Science of Alloys for the 21st Century: A Hume-Rothery Symposium Celebration*, The Minerals, Metals, and Materials Society, Warrendale, PA.

Johnson, W. L. 1999, *MRS Bull. 24*, 42.

Kronberg, M. L.; Wilson, F. H. 1949, *Trans. Met. Soc. AIME*, *185*, 501.

Mayer, T. M.; Adams, D. P.; Swartzentruber, 1994, "Nucleation and Evolution of Film Structure in Chemical Vapor Deposition Processes," *Physical and Chemical Sciences Center Research Briefs*, Vol. 1-96, Sandia National Laboratories.

Mott, N. F. 1948, *Proc. Phys. Soc. London.*, *60*, 391.

Movchan, B. A.; Demchishin, A. V. 1969, *Phys. Met. Metallogr.*, *28*, 83.

Muller, C.; Chateigner, D.; Anne, M.; Bacmann, M.; Fouletier, J.; de Rango, P. 1996, *J. Phys. D*, *29*, 3106.

Mullins, W. W.; Sekerka, R. F. 1963, *J. Appl. Phys.*, *34*, 323.

Palumbo, G.; Lehockey, E. M.; Lin, P. 1998, *JOM*, *50*(*2*), 40.

Perker, A.; Johnson, W. L. 1993, *Appl. Phys. Lett.*, *63*, 2342.

Phanikumar, G.; Chattopadhyay. 2001, *Sadhana*, *26*, 25.

Randle, V. 1993, *The Measurement of Grain Boundary Geometry*, IOP Publishing, Ltd., London.

Ranganathan, S. 1966, *Acta Crystallogr.*, *21*, 197.

Read, W. T.; Shockley. W. 1950, *Phys. Rev.*, *78*, 275.

Salvador, P. A.; Doan, T. D.; Mercey, B.; Raveau, B. 1998, *Chem. Mater*, *10*, 2592.

Saylor, D. M.; Morawiec, A.; Adams, B. L.; Rohrer, G. S. 2000, *Interface Sci.*, *8*[*2/3*], 131.

Scheil, E. Z. 1942, *Metallkunde*, *34*, 70.

Stauffer, D.; Aharony, A. 1994, *Introduction to Percolation Theory,* rev. 2nd ed., Taylor & Francis, London, p. 52.

Tammann, G. Z. 1904, *Elektrochem.*, *10*, 532.

Thaveepringsriporn, V.; Was, G. S. 1997, *Metall. Trans. A*, *28*, 2101.

Thornton, J. A. 1977, *Ann. Rev. Mater. Sci.*, *7*, 239.

Tiller, W. A.; Jackson, K. A.; Rutter, R. W.; Chalmers, B., 1953, *Acta Metall. 1*, 50.

Turnbull, D.; Fisher, J. 1949, *J. Chem. Phys.*, *17*, 71.

Turnbull, D. 1950, *J. Chem. Phys.*, *18*, 198.

Turnbull, D. 1981, *Met. Trans. A*, *12*, 695.

Was, G. S., Thaveepringsriporn, V.; Crawford, D. C. 1998, *JOM*, *50*, 44.

Watanabe, T. 1984, *Res. Mech. 11*, 47.

Watanabe, T. 1993, In: Erb, U., Palumbo, G., editors, *Grain Boundary Engineering*, CIM, Montreal.

Weertman, J.; Weertman, J. R. 1992, *Elementary Dislocation Theory,* Oxford University Press, New York, p. 6.

Wolf, D.; Lutsko, J. F. 1989, *Z. Kristall.*, *189*, 239.

Yamaura, S.; Igarashi, Y.; Tsurekawa, S, Watanabe, T. 2000. In: Meike, A., Gonis, A., Turchi, P. E. A., Rajan, K., editors, *Properties of Complex Inorganic Solids 2*, Kluwer Academic/Plenum Publishers, New York, pp. 27–37.